Monthly Notices of the ROYAL ASTRONOMICAL SOCIETY

MNRAS **520,** 6173–6189 (2023) https://doi.org/10.1093/mnras/stad389
Advance Access publication 2023 February 3

Multimessenger emission from tidal waves in neutron star oceans

Andrew G. Sullivan [1]★ Lucas M. B. Alves [1] Georgina O. Spence,[2] Isabella P. Leite [3] Doğa Veske [1] Imre Bartos [4] Zsuzsa Márka [5] and Szabolcs Márka [1]

[1]*Department of Physics, Columbia University in the City of New York, New York, NY 10027, USA*
[2]*Department of Mathematics, Barnard College of Columbia University in the City of New York, New York, NY 10027, USA*
[3]*Department of Biomedical Engineering, Columbia University in the City of New York, New York, NY 10027, USA*
[4]*Department of Physics, University of Florida, Gainesville, FL 32611-8440, USA*
[5]*Columbia Astrophysics Laboratory, Columbia University in the City of New York, New York, NY 10027, USA*

Accepted 2023 January 31. Received 2023 January 9; in original form 2022 June 3

ABSTRACT

Neutron stars in astrophysical binary systems represent exciting sources for multimessenger astrophysics. A potential source of electromagnetic transients from compact binary systems is the neutron star ocean, the external fluid layer encasing a neutron star. We present a groundwork study into tidal waves in neutron star oceans and their consequences. Specifically, we investigate how oscillation modes in neutron star oceans can be tidally excited during compact binary inspirals and parabolic encounters. We find that neutron star oceans can sustain tidal waves with frequencies between 0.01 and 20 Hz. Our results suggest that tidally resonant neutron star ocean waves may serve as a never-before studied source of precursor electromagnetic emission prior to neutron star–black hole and binary neutron star mergers. If accompanied by electromagnetic flares, tidally resonant neutron star ocean waves, whose energy budget can reach 10^{46} erg, may serve as early warning signs ($\gtrsim$1 min before merger) for compact binary mergers. Similarly, excited ocean tidal waves will coincide with neutron star parabolic encounters. Depending on the neutron star ocean model and a flare emission scenario, tidally resonant ocean flares may be detectable by *Fermi* and Nuclear Spectroscopic Telescope Array (*NuSTAR*) out to $\gtrsim$100 Mpc with detection rates as high as $\sim$7 yr^{-1} for binary neutron stars and $\sim$0.6 yr^{-1} for neutron star–black hole binaries. Observations of emission from neutron star ocean tidal waves along with gravitational waves will provide insight into the equation of state at the neutron star surface, the composition of neutron star oceans and crusts, and neutron star geophysics.

Key words: gravitational waves – stars: oscillations – X-rays: bursts – black hole - neutron star mergers – neutron star mergers.

1 INTRODUCTION

With the recent detections of gravitational waves (GWs) from compact binary systems by GW detectors such as Laser Interferometer Gravitational Wave Observatory (LIGO), Virgo, and KAGRA (Acernese et al. 2015; LIGO Scientific Collaboration 2015; LIGO Scientific Collaboration & Virgo Collaboration 2017, 2021; Akutsu et al. 2019; LIGO Scientific Collaboration, Virgo Collaboration & Kamioka Gravitational Wave Detector (KAGRA) Collaboration 2021), binary systems that include neutron stars have come to the forefront of high-energy astrophysics. Neutron stars represent a unique class of stellar objects in that, though very dense, they emit light, making them a candidate for combined GW–electromagnetic multimessenger astrophysical searches (Rosswog 2015; Abbott et al. 2018). Neutron stars are thought to consist of three distinct layers: a very dense fluid core, a solid crust, and an external fluid ocean (Lattimer & Prakash 2001). The respective properties of each of these layers largely depend on the neutron star equation of state (Lattimer & Prakash 2001), whose details remain an active problem in nuclear physics and astrophysics. Detections of X-ray bursts (Bildsten & Cutler 1995; Strohmayer & Mahmoodifar 2014; Chambers & Watts 2020), gamma-ray bursts (Tsang et al. 2012; Tsang 2013; Suvorov & Kokkotas 2020), ejecta from compact binary inspirals (Metzger et al. 2010; Metzger & Fernández 2014; Chornock et al. 2017; Cowperthwaite et al. 2017; Geroyannis, Tzelati & Karageorgopoulos 2017; Metzger 2017; Nicholl et al. 2017; Soares-Santos et al. 2017; Radice et al. 2018; Bartos & Marka 2019; Metzger 2019), and GWs (Andersson & Kokkotas 1998; Ferrari 2010; Suvorov 2018; Chatziioannou 2020) may probe this structure.

In recent years, GW astrophysics has become a unique observational tool to study neutron star physics. The answers to a number of open questions concerning the properties of neutron stars may lie in the rich capabilities of multimessenger astrophysics with GWs. Works have investigated the possibility of mountains on the surfaces of spinning neutron stars, whose asymmetries could generate detectable continuous GWs (Ushomirsky, Cutler & Bildsten 2000; Osborne & Jones 2020; Gittins & Andersson 2021; Gittins, Andersson & Jones 2021). Searches for continuous GWs potentially originating from spinning neutron stars have been undertaken (Aasi et al. 2015; Papa et al. 2020; LIGO Scientific Collaboration, Virgo Collaboration & KAGRA Collaboration 2022a, 2022b; Abbott et al. 2022), and may study neutron star geophysical structure

★ E-mail: ags2198@columbia.edu

and seismology (Geroyannis et al. 2017; Suvorov 2018; Yang et al. 2018; Andersson 2021). Neutron stars exhibit a variety of pulsational modes (McDermott, van Horn & Hansen 1988; Lai 1994; Reisenegger & Goldreich 1994; Passamonti et al. 2006; Samuelsson, Andersson & Maniopoulou 2007; Passamonti & Andersson 2012). These oscillation modes are associated with the restoring forces and structure of the star. Modes include the fundamental mode or f mode (Lau, Leung & Lin 2010; LIGO Scientific Collaboration & Virgo Collaboration 2017; Wen et al. 2019; LIGO Scientific Collaboration, Virgo Collaboration & KAGRA Collaboration 2021), pressure modes or p modes (Bandari 2014), gravity modes or g modes (McDermott et al. 1988; Bildsten & Cutler 1995; Bildsten, Ushomirsky & Cutler 1996; Deibel 2016; Andersson & Pnigouras 2020; Kuan, Suvorov & Kokkotas 2021a; Passamonti, Andersson & Pnigouras 2021), r modes in rotating neutron stars (Haskell 2015; Mitidis 2015; Chambers & Watts 2020; Ma, Yu & Chen 2021), and interface modes or i modes (McDermott et al. 1988; Passamonti & Andersson 2012). Oscillation modes may be excited during accretion (Reisenegger & Goldreich 1994; Deibel 2016) or by tides (Lai 1994; Ho & Lai 1999; Gittins et al. 2021).

Neutron star oscillations have been studied in connection with emission of electromagnetic radiation. The prospect of observing neutron star ocean oscillations induced by accretion, in particular, has been considered in many previous works (Bildsten & Cutler 1995; Bildsten et al. 1996; Heyl 2004; Deibel 2016; Chambers & Watts 2020; van Baal, Chambers & Watts 2020). Thermonuclear burning on neutron star surfaces during accretion can excite oscillation modes, which could represent the oscillations in type I X-ray burst light curves (Hansen & van Horn 1975; Woosley & Taam 1976; Maraschi & Cavaliere 1977; Bildsten & Cutler 1995; Spitkovsky, Levin & Ushomirsky 2002; Lee 2004; Piro & Bildsten 2005b; Chambers et al. 2018; Chambers & Watts 2020). Observed thermonuclear X-ray bursts on neutron stars show signs of ocean mode oscillation (Galloway et al. 2008; Bilous & Watts 2019; Bult et al. 2021; Roy, Beri & Bhattacharyya 2021).

Because neutron stars can exist in binaries, tidal deformations play a role in neutron star physics as well. A neutron star's response to tidal forces largely depends on its internal properties, including its oscillation modes (Lai 1994). Observations of tidally excited oscillation modes would probe the composition of neutron stars.

In this work, we analyse neutron star ocean oscillations generated by the dynamical tide during interactions with other compact objects. We principally consider ocean tidal waves in compact binary inspirals, where tidal forces become resonant with neutron star oceans. We also investigate tidal waves from unbound neutron star encounters. We present models for neutron star oceans and investigate the size of tidal waves sustainable in these oceans. Ultimately, we consider astrophysical emission that tidally excited neutron star oceans might produce, including electromagnetic flares and GWs. We perform all of our analysis using Newtonian theory due to the exploratory and phenomenological nature of this study.

We divide the paper into the following sections. In Section 2, we present the background neutron star model used, as well as introduce the three neutron star ocean models investigated. In Section 3, we discuss the equations of motion for neutron star oscillations and determine the neutron star ocean oscillation modes for our models. In Section 4, we discuss the tidal interaction and compute tidal wave properties for each of the oceans and orbital configurations considered. In Section 5, we discuss our results and their consequences, including potential emission produced by neutron star ocean tidal waves. In Section 6, we conclude.

2 BACKGROUND NEUTRON STAR AND OCEAN MODEL

To focus on the properties of the neutron star ocean, we use a simple background neutron star model with a rigid crust. We will later extrapolate our results with this model to the case where the neutron star crust is elastic rather than rigid.

To solve for the star's background density ρ and pressure p, we use the classical equilibrium equations for a spherically symmetric fluid:

$$\frac{\mathrm{d}p}{\mathrm{d}r} = -\rho g, \tag{1a}$$

$$\frac{\mathrm{d}M}{\mathrm{d}r} = 4\pi G r^2 \rho, \tag{1b}$$

where $M(r)$ is the mass enclosed at a given radius, G is Newton's gravitational constant, and $g = \frac{GM(r)}{r^2}$ (Chandrasekhar 1957). Given an equation of state, these equations can be solved and provide the star's background pressure and density. In this work, we use a polytropic equation of state (Ferrari, Rossi & Malheiro 2010):

$$p = K\rho^{\Gamma}, \tag{2}$$

where K is a proportionality constant. Choosing $\Gamma = 2$ yields an analytic solution for the mass density when $r < R_\star$.

$$\rho(r) = \rho_{\mathrm{c}} \frac{\sin\sqrt{\frac{4\pi G}{2K}}r}{\sqrt{\frac{4\pi G}{2K}}r}, \tag{3}$$

where ρ_{c} is the density at the centre of the star and $R_\star$ is the radius of the neutron star (Chandrasekhar 1957). When $r > R_\star$, we have $\rho(r) = 0$. Note that the radius of the star is completely specified by the constant K.

For this study, we assume that our neutron star is non-rotating and has no magnetic field. The effects of rotation and magnetization, if small enough, will serve as perturbations to the oscillation mode structures and frequencies without changing the physics (Krüger et al. 2021; Kuan, Suvorov & Kokkotas 2021b,). Because we are interested in early inspirals, the effects of general relativity should not play a role in spinning up the rotation of neutron stars. While we expect effects such as tidal locking to also spin up neutron stars, we do not consider them in our study. We leave consideration of rotating and magnetized neutron stars to future work.

2.1 Neutron star ocean depth

The depth of the neutron star ocean depends on the density at which the neutron star crust melts. The top of the crust is typically considered to be a body-centred cubic Coulomb crystal (Bildsten & Cutler 1995; Haensel, Potekhin & Yakovlev 2007; Horowitz & Kadau 2009; Baiko & Chugunov 2018; Gittins, Andersson & Pereira 2020). In a Coulomb crystal, the ions that compose the lattice interact exclusively by the Coulomb interaction (Chambers et al. 2018) because the electron screening in the outer crust is weak (Chamel & Haensel 2008). The Coulomb crystal undergoes a phase transition when the thermal energy exceeds the electric binding energy of the material by some critical factor γ (Farouki & Hamaguchi 1993). The

crust melts when the following condition is met:

$$k_{\rm B}T \geq \frac{1}{\gamma}\frac{1}{4\pi\epsilon_0}\frac{Z^2e^2}{d}, \tag{4}$$

where $k_{\rm B}$ is Boltzmann constant, T is the temperature, ϵ_0 is the permittivity of free space, Z is the proton number of atomic nuclei in the lattice, e is electron charge, and d is the mean spacing between nuclei. Molecular dynamics studies have found $\gamma \approx 173$ (Farouki & Hamaguchi 1993). Assuming that the ion number density is $n_{\rm i} = (\frac{4}{3}\pi d^3)^{-1}$, the mass density at which the crust melts and the ocean forms is

$$\begin{aligned}\rho_{\rm o} &= Am_{\rm n}n_{\rm i} = \frac{3}{4\pi}Am_{\rm n}\left(\gamma\frac{4\pi\epsilon_0 k_{\rm B}T}{Z^2e^2}\right)^3 \\ &\approx 2.705\times10^{10}\ {\rm g\ cm^{-3}}\left(\frac{A}{16}\right)\left(\frac{8}{Z}\right)^6\left(\frac{T}{10^8\ {\rm K}}\right)^3,\end{aligned} \tag{5}$$

where A is the atomic mass of the nuclei in the lattice, $m_{\rm n}$ is nucleon mass, and we have used the condition in equation (4) for d at the transition between the neutron star crust and ocean. Equation (5) shows the melting density's strong dependence on temperature and ion atomic number. More proton-rich nuclei will reduce the density at which the ocean begins.

By plugging equation (5) into the left-hand side of equation (3), we determine the radius at which the ocean begins and by extension the depth of the ocean as a function of A, Z, and T when $\Gamma = 2$. Since the ocean is very shallow compared to the neutron star radius (Bildsten & Cutler 1995; Bildsten et al. 1996; Urpin 2004; Deibel 2016; van Baal et al. 2020), we approximate r in the denominator of equation (3) as the stellar radius $R_\star = \sqrt{\frac{2K}{4\pi G}}\frac{\pi}{2}$. The radius at which the neutron star ocean begins for a $\Gamma = 2$ polytropic equation of state is

$$r_{\rm o} = \sqrt{\frac{2K}{4\pi G}}\left[\arccos\left(\frac{3}{8}\frac{Am_{\rm n}}{\rho_{\rm c}}\left(\gamma\frac{4\pi\epsilon_0 k_{\rm B}T}{Z^2e^2}\right)^3\right)+\frac{\pi}{2}\right]. \tag{6}$$

We also obtain an approximate ocean depth $h_{\rm o}$ for a general polytropic equation of state in terms of $\rho_{\rm o}$. Differentiating equation (2) gives

$$\frac{{\rm d}p}{{\rm d}r} = \Gamma K\rho^{\Gamma-1}\frac{{\rm d}\rho}{{\rm d}r}. \tag{7}$$

Combining equations (1a) and (7) provides a differential equation for ρ and r:

$$\frac{{\rm d}\rho}{{\rm d}r} = -\frac{g}{\Gamma K}\rho^{2-\Gamma}. \tag{8}$$

Integrating equation (8) from the ocean floor to the surface assuming constant $g = \frac{GM}{R_\star^2}$ gives

$$h_{\rm o} = R_\star - r_{\rm o} = \frac{\Gamma K}{\Gamma-1}\frac{\rho_{\rm o}^{\Gamma-1}}{g}. \tag{9}$$

Any choice of K and Γ in the ocean can therefore give an approximate $h_{\rm o}$.

In this work, we consider three model crusts, respectively, made up of three elements thought to be found in neutron star surfaces due to their production by r-processes (Meisel et al. 2018): carbon with $Z = 6$ and $A = 12$, oxygen with $Z = 8$ and $A = 16$, and iron with $Z = 26$ and $A = 56$. For referential convenience, we refer to the three oceans corresponding to these differently composed crusts as carbon, oxygen, and iron oceans, respectively. Neutron star crust temperatures are typically $T \sim 10^7$ K when the crust is in thermal equilibrium with the core (Brown, Bildsten & Rutledge 1998; Brown & Cumming 2009). Accretion can raise the temperature of the neutron star ocean floor to $T \sim 10^8$ K (Fujimoto et al. 1984; Haensel & Zdunik 1990, 2003, 2008). The temperature decreases through the ocean to 10^6 K at the surface (Miralda-Escude, Haensel & Paczynski 1990; Chamel & Haensel 2008). In our study, we neglect effects of the ocean temperature gradient. We discuss our choice for crust temperature in Section 3.4.1.

3 NEUTRON STAR OCEAN OSCILLATION MODES

We solve for the dynamical response of the neutron star ocean. To do this, we use the formalism of Lagrangian perturbation theory for fluids (Friedman & Schutz 1978). Using the Newtonian formalism typically used, we solve for the oscillation modes of the neutron star ocean (Dziembowski 1971; Ledoux 1974; McDermott et al. 1988; Passamonti & Andersson 2012), so that we may study the dynamical response to tidal forces (Lai 1994; Reisenegger & Goldreich 1994; Tsang et al. 2012; Tsang 2013; Passamonti et al. 2021).

3.1 Equations of motion

The equation of motion for Lagrangian perturbative displacements is the perturbed Euler equation

$$\partial_t^2\boldsymbol{\xi} + \frac{\nabla\delta p}{\rho} - \frac{\delta\rho}{\rho^2}\nabla p + \nabla\delta\phi - \frac{1}{\rho}\nabla\cdot\boldsymbol{\sigma} = -\nabla\chi, \tag{10}$$

where $\boldsymbol{\xi}$ is the Lagrangian displacement vector, ρ is the background fluid density, p is the background fluid pressure, $\delta\rho$ is the Eulerian perturbation of the density, δp is the Eulerian perturbation of the pressure, $\delta\phi$ is the Eulerian perturbation of the gravitational potential, $\boldsymbol{\sigma} = \sigma_{ij}$ is the elastic stress tensor, and χ is an unspecified (for now) external potential that drives the system. The elastic stress tensor is defined as

$$\sigma_{ij} = \breve{\mu}\left(\nabla_i\xi_j + \nabla_j\xi_i\right) - \frac{2}{3}\breve{\mu}\delta_{ij}\left(\nabla\cdot\boldsymbol{\xi}\right), \tag{11}$$

where $\breve{\mu}$ is the shear modulus and δ_{ij} is the Kronecker delta. In a fluid, $\breve{\mu} = 0$.

The Lagrangian perturbation for density can be written as

$$\Delta\rho = \delta\rho + \boldsymbol{\xi}\cdot\nabla\rho = -\rho\nabla\cdot\boldsymbol{\xi}, \tag{12}$$

where the first equality is the definition of the Lagrangian perturbation in terms of the Eulerian perturbation and the second equality arises from conservation of mass (Friedman & Schutz 1978). If the oscillations are adiabatic, the Lagrangian perturbations for pressure and density are related by

$$\frac{\Delta\rho}{\rho} = \frac{1}{\Gamma_1}\frac{\Delta p}{p}, \tag{13}$$

where Γ_1 is the adiabatic index. We note that Γ_1 does not necessarily equal Γ. When $\Gamma_1 \neq \Gamma$, the neutron star is stratified and can sustain internal g modes (McDermott et al. 1988; Bildsten & Cutler 1995; Bildsten et al. 1996; Andersson & Pnigouras 2020; Passamonti et al. 2021).

The final equation of motion that governs this system is the perturbative form of the Poisson equation

$$\nabla^2\delta\phi = 4\pi G\delta\rho. \tag{14}$$

Since the ocean is the uppermost layer of the star and typically very shallow, the perturbation of the gravitational potential $\delta\phi$ and its gradient $\nabla\delta\phi$ must be very small compared to the background gravitational potential ϕ and the background gravitational acceleration

g. As such, we employ the Cowling approximation (Cowling 1941), which approximates $\delta\phi \approx 0$ and $\nabla\delta\phi \approx 0$. Consequently, we neglect the appearance of $\delta\phi$ in equation (10).

In this section, we set $\chi = 0$ and study the homogeneous solutions to equation (10). First, we define a perturbation to the chemical potential per nucleon mass $\delta\tilde{\mu}$, which, in a barotropic fluid where $\Gamma = \Gamma_1$, is related to the perturbation of pressure by

$$\delta p = n_{\rm N}\delta\mu = \rho\delta\tilde{\mu}, \tag{15}$$

where $\delta\mu$ is the normal chemical potential, and $n_{\rm N}$ is the nucleon number density. Inserting equation (15) for δp into equation (10), explicitly writing out the derivative of the stress tensor, and applying the Cowling approximation gives

$$\begin{aligned} 0 = {} & \partial_t^2\boldsymbol{\xi} + \nabla\delta\tilde{\mu} \\ & - \frac{1}{\rho}\left(\frac{\mathrm{d}\breve{\mu}}{\mathrm{d}r}(\nabla_r\boldsymbol{\xi} + \nabla\xi_r) + \breve{\mu}\left(\nabla(\nabla\cdot\boldsymbol{\xi}) + \nabla^2\boldsymbol{\xi}\right)\right. \\ & \left. - \frac{2}{3}\nabla(\breve{\mu}\nabla\cdot\boldsymbol{\xi})\right). \end{aligned} \tag{16}$$

We use equations (12) and (13) to obtain the other equation we need to solve this system. From the definition of the Lagrangian perturbation (Friedman & Schutz 1978), we have

$$\Delta p = \delta p + \boldsymbol{\xi}\cdot\nabla p = \rho\delta\tilde{\mu} + \xi_r\frac{\mathrm{d}p}{\mathrm{d}r}, \tag{17}$$

where ξ_r is the radial component of $\boldsymbol{\xi}$ and the second equality comes from equation (15) and spherical symmetry (i.e. $\nabla p = \frac{\mathrm{d}p}{\mathrm{d}r}$). Substituting equations (17) and (12) into equation (13), we obtain

$$\nabla\cdot\boldsymbol{\xi} = -\frac{1}{\Gamma_1 p}\left(\rho\delta\tilde{\mu} + \xi_r\frac{\mathrm{d}p}{\mathrm{d}r}\right). \tag{18}$$

Equations (16) and (18) are a system of partial differential equations, which can be solved using a clever ansatz for $\boldsymbol{\xi}$. We decompose $\boldsymbol{\xi}$ into normal modes (Dziembowski 1971; Ledoux 1974; McDermott et al. 1988; Passamonti & Andersson 2012):

$$\boldsymbol{\xi} = \sum_n \mathrm{e}^{\mathrm{i}\omega_n t}\boldsymbol{\xi}_n, \tag{19}$$

where ω_n is the angular frequency of a resonant mode and $\boldsymbol{\xi}_n$ is the eigenfunction that solves the equation

$$(\mathcal{L} - \rho\omega_n^2)\boldsymbol{\xi_n} = 0, \tag{20}$$

where $\mathcal{L}$ is an operator defined such that $\mathcal{L}\boldsymbol{\xi} = \rho\nabla\delta\tilde{\mu} - \nabla\cdot\boldsymbol{\sigma}$ (Press & Teukolsky 1977; Passamonti et al. 2021). The index n denotes the mode. The orthogonality of these modes requires (Press & Teukolsky 1977; Lai 1994; Passamonti et al. 2021)

$$\langle\boldsymbol{\xi}_n|\boldsymbol{\xi}_m\rangle = \int \rho\boldsymbol{\xi}_n^*\cdot\boldsymbol{\xi}_m\mathrm{d}V = A_n^2\delta_{nm}, \tag{21}$$

where the integral is over the volume of the star, $\boldsymbol{\xi}_n^*$ is the complex conjugate of $\boldsymbol{\xi}_n$, and A_n^2 is the normalization factor. The spherical symmetry of the problem allows us to write $\boldsymbol{\xi}_n$ as (Dziembowski 1971; Ledoux 1974; McDermott et al. 1988; Passamonti & Andersson 2012)

$$\boldsymbol{\xi}_n = \left(U(r)Y_{lm}(\theta,\phi),\, V(r)\partial_\theta Y_{lm}(\theta,\phi),\, \frac{V(r)}{\sin\theta}\partial_\phi Y_{lm}(\theta,\phi)\right), \tag{22}$$

where $Y_{lm}(\theta,\phi)$ are the spherical harmonic functions (Jackson 1962), ∂_x is the partial derivative with respect to the variable x, and $U(r)$ and $V(r)$ are functions of the radial coordinate that must be solved for. The spherical symmetry also allows us to write $\delta\tilde{\mu}$ as $\delta\tilde{\mu} = \delta\tilde{\mu}(r)Y_{lm}(\theta,\phi)\mathrm{e}^{\mathrm{i}\omega t}$.

3.1.1 *Fluid ocean*

In the fluid components of the neutron star where $\breve{\mu} = 0$, equation (16) simplifies considerably. With spherical symmetry and $\breve{\mu} = 0$, equations (16) and (18) become first-order ordinary differential equations in the radial coordinate r

$$-\omega^2 U + \frac{\mathrm{d}}{\mathrm{d}r}\delta\tilde{\mu} = 0, \tag{23a}$$

$$-\omega^2 V + \frac{\delta\tilde{\mu}}{r} = 0, \tag{23b}$$

$$\frac{\mathrm{d}U}{\mathrm{d}r} + \frac{2}{r}U - \frac{l(l+1)}{r}V = -\frac{1}{\Gamma_1 p}\left(\rho\delta\tilde{\mu} + U\frac{\mathrm{d}p}{\mathrm{d}r}\right). \tag{23c}$$

These equations are valid in the fluid neutron star ocean. Rearranging equations (23a) and (23c) and using the relationship in equation (23b), this system reduces to two ordinary differential equations:

$$\frac{\mathrm{d}}{\mathrm{d}r}\delta\tilde{\mu} = \omega^2 U, \tag{24a}$$

$$\frac{\mathrm{d}U}{\mathrm{d}r} = -\left(\frac{2}{r} + \frac{1}{\Gamma_1 p}\frac{\mathrm{d}p}{\mathrm{d}r}\right)U + \left(-\frac{\rho}{\Gamma_1 p} + \frac{l(l+1)}{r^2\omega^2}\right)\delta\tilde{\mu}. \tag{24b}$$

We write these equations in terms of the dimensionless variables $y_1 = \frac{U}{r}$ and $y_2 = \frac{\delta\tilde{\mu}}{rg}$, where g is the background gravitational field as a function of radius. We obtain

$$\frac{\mathrm{d}y_1}{\mathrm{d}r} = -\left(\frac{3}{r} + \frac{1}{\Gamma_1 p}\frac{\mathrm{d}p}{\mathrm{d}r}\right)y_1 + \left(-\frac{\rho}{\Gamma_1 p} + \frac{l(l+1)}{r^2\omega^2}\right)g y_2, \tag{25a}$$

$$\frac{\mathrm{d}y_2}{\mathrm{d}r} = \frac{\omega^2}{g}y_1 - \left(\frac{1}{r} + \frac{1}{g}\frac{\mathrm{d}g}{\mathrm{d}r}\right)y_2. \tag{25b}$$

In the single fluid limit and the Cowling approximation, the equations in section A1 of Passamonti & Andersson (2012) reduce to equation (25). Given boundary conditions at the ocean–crust interface and ocean surface, a value for Γ_1 (which is not constant in general), and a value of l, we may solve these equations as a boundary value problem.

3.1.2 *Elastic crust*

If the crust is elastic, the ocean oscillation modes may penetrate into the crust, requiring one to solve equation (16) when $\breve{\mu} \neq 0$ (Piro & Bildsten 2005a). In this work, rather than solving equations (16) and (18) in the elastic crust, we will solve for modes in the ocean assuming a rigid crust and extrapolate our results from the rigid to the elastic case, focusing particularly on the consequences for the neutron star tide.

3.2 Boundary conditions

In this work, we solve equation (23) assuming that the mode is entirely confined to the ocean. For this simple case, oscillations do not penetrate into the crust. At the ocean floor, we apply the condition

$$y_1(r_{\rm o}) = 0. \tag{26}$$

This is the same condition applied by Bildsten & Cutler (1995) to solve for deep ocean g modes. At the surface of the ocean, we apply the condition $\Delta p = 0$ (McDermott et al. 1988; Lai 1994). In our variables, this becomes

$$0 = y_1(R_\star) - y_2(R_\star). \tag{27}$$

Additionally, so that we can find the functional form of the oscillation modes, we apply a normalization condition at the surface of the

ocean,

$$y_1(R_\star) = 1. \tag{28}$$

With these three boundary conditions, our system is closed and solvable. We note that equation (26) only preserves continuity of the radial displacement if there is no radial displacement in the crust. This is not necessarily a suitable boundary condition for an elastic crust as the true ocean–crust junction condition is the continuity of the radial displacement and traction variables (McDermott et al. 1988; Passamonti & Andersson 2012; Passamonti et al. 2021). For a more detailed treatment including the mode's penetration into the crust, one must impose these conditions.

3.3 Semi-analytic ocean modes and tidal resonance

We now provide a simple analytic argument to demonstrate the existence of ocean modes and estimate how the ocean mode frequency scales with model parameters in both the rigid crust and elastic crust cases. This will also give the time of tidal resonance as a function of model parameters.

3.3.1 Shallow ocean surface wave model

Treating the neutron star ocean as an incompressible shallow ocean, we analytically estimate the neutron star ocean mode frequencies. For waves in a shallow ocean, one solves for the height of the wave above the ocean surface η. In an incompressible fluid, the density ρ is not a function of the pressure, so the pressure is often taken to be $p = \rho g(h_f - z)$, where h_f is the total height of the ocean. When the height is perturbed by surface waves, we have $h_f = h_\mathrm{o} + \eta$, where h_o is the equilibrium depth of the ocean. For waves with $\eta << h_\mathrm{o}$, the perturbed Euler equation and the continuity equation become

$$\partial_t \boldsymbol{v}_\mathrm{H} = -\frac{\nabla_\mathrm{H}\delta p}{\rho}, \tag{29a}$$

$$\rho\partial_t\eta + \rho h_\mathrm{o}\nabla_\mathrm{H}\cdot\boldsymbol{v}_\mathrm{H} = 0, \tag{29b}$$

where $\boldsymbol{v}_\mathrm{H} = (v_x, v_y)$ is the fluid velocity in the horizontal direction, the gradient $\nabla_\mathrm{H} = (\partial_x, \partial_y)$ is the gradient in the horizontal direction, and δp is the perturbation to the pressure due to the wave (Randall 2006).

Because $h_f = h_\mathrm{o} + \eta$ for a perturbed ocean, we have $p + \delta p = \rho g(h_\mathrm{o} + \eta - z)$. $p = \rho g(h_\mathrm{o} - z)$ is the background pressure, so the perturbation to the pressure is $\delta p = \rho g\eta$. Equation (29a) becomes

$$\partial_t \boldsymbol{v}_\mathrm{H} = -g\nabla_\mathrm{H}\eta. \tag{30}$$

Taking the divergence of equation (30) gives

$$\partial_t(\nabla_\mathrm{H}\cdot\boldsymbol{v}_\mathrm{H}) = -g\nabla_\mathrm{H}^2\eta. \tag{31}$$

Dividing out the mass density and taking the time derivative of equation (29b) gives

$$\partial_t^2\eta + h_\mathrm{o}\partial_t(\nabla_\mathrm{H}\cdot\boldsymbol{v}_\mathrm{H}) = 0. \tag{32}$$

Combining equations (31) and (32) gives the wave equation for the height of the wave η:

$$\partial_t^2\eta - gh_\mathrm{o}\nabla_\mathrm{H}^2\eta = 0. \tag{33}$$

At this point, we reintroduce the spherical nature of this problem by assuming $\eta = \eta(t)Y_{lm}$. In spherical coordinates, this problem becomes that of an incompressible fluid shell surrounding a sphere of radius $R_\star$, similar to a neutron star ocean. While we have previously been working in Cartesian coordinates, the wave equation for η holds in spherical coordinates if η is not a function of r. Expanding η in spherical harmonics, equation (33) becomes

$$\partial_t^2\eta + \frac{l(l+1)}{R_\star^2}gh_\mathrm{o}\eta = 0. \tag{34}$$

We arrive at ocean mode frequencies in an incompressible fluid ocean surrounding a spherical body of radius $R_\star$ as

$$\omega_i = \frac{1}{R_\star}\sqrt{l(l+1)gh_\mathrm{o}} = \sqrt{l(l+1)\frac{GM_\star}{R_\star^3}\frac{h_\mathrm{o}}{R_\star}}, \tag{35}$$

where the subscript i refers to incompressibility. To obtain intuition about the functional dependence of the real ocean mode frequencies on our model parameters, we substitute equation (9) for h_o in equation (35) and obtain

$$\omega \sim \frac{1}{R_\star}\sqrt{l(l+1)\frac{K\Gamma}{\Gamma-1}\rho_\mathrm{o}^{\Gamma-1}}, \tag{36}$$

where we have replaced the equal sign with a tilde for more realistic neutron star oceans. We now substitute in the expression for ρ_o from equation (5) to obtain

$$\omega \sim \frac{1}{R_\star}\sqrt{\frac{l(l+1)K\Gamma}{\Gamma-1}}\left(\gamma\left(\frac{3}{4\pi}m_\mathrm{n}\right)^{\frac{1}{3}}\frac{4\pi\epsilon_0 k_\mathrm{B}}{e^2}\right)^{\frac{3\Gamma-3}{2}} \times A^{\frac{\Gamma-1}{2}}Z^{3-3\Gamma}T^{\frac{3\Gamma-3}{2}}. \tag{37}$$

Equation (37) estimates the mode frequency when the crust is taken to be rigid. One can see that the mode frequency increases as a function of T and A and decreases as a function of Z for $\Gamma > 1$.

Piro & Bildsten (2005a) showed that if the pressure at the crust–ocean interface p_o exceeds the shear modulus $\breve{\mu}$, one cannot treat this mode as purely a shallow ocean surface wave, but rather as an interface mode with a non-zero $\boldsymbol{\xi}$ in the crust. The interface mode frequency will be the shallow ocean mode frequency scaled by $\sqrt{\frac{\breve{\mu}}{p_\mathrm{o}}}$:

$$\omega \sim \left(\frac{\breve{\mu}}{p_\mathrm{o}}\right)^{\frac{1}{2}}\frac{1}{R_\star}\sqrt{\frac{l(l+1)K\Gamma}{\Gamma-1}}\left(\gamma\left(\frac{3}{4\pi}m_\mathrm{n}\right)^{\frac{1}{3}}\frac{4\pi\epsilon_0 k_\mathrm{B}}{e^2}\right)^{\frac{3\Gamma-3}{2}} \times A^{\frac{\Gamma-1}{2}}Z^{3-3\Gamma}T^{\frac{3\Gamma-3}{2}}. \tag{38}$$

Consequently, when the ocean has an elastic crust, equation (38) approximates the ocean mode frequency.

These expressions show the functional dependence of the mode on parameters of the model. Such modes have been shown to exist in non-homogenous atmospheres as well (Taylor 1936). This analysis demonstrates the capacity of oceans to sustain modes with lower frequencies than the neutron star f mode (McDermott et al. 1988; Passamonti et al. 2021, for example) regardless of ocean stratification.

3.3.2 Tidal resonance estimates

Since we are interested in tidal resonances during compact binary inspirals, we estimate the time before compact binary merger of an ocean tidal resonance. Tidal resonances should occur when

$$\dot{\Phi} = \frac{\omega}{m}, \tag{39}$$

where $\dot{\Phi}$ is the orbital frequency of the compact binary and m is the spherical harmonic index. For circular binaries, we have

$$\dot{\Phi} = \sqrt{\frac{G(M + M_*)}{D^3}}, \tag{40}$$

where M_* is the mass of the companion object and D is orbital separation. The time to merger for a given orbital separation D is (Peters 1964)

$$t_m = \frac{D^4}{4\beta}, \tag{41}$$

where β is

$$\beta = \frac{64}{5}\frac{G^3 M M_*(M + M_*)}{c^5}, \tag{42}$$

where c is the speed of light. Combining equations (37), (39), (40), and (41) gives an expression for the time before merger when resonance occurs (hereafter resonance time) in the rigid crust case as

$$t_r \sim \frac{1}{4\beta}\left(\frac{R_\star^2 m^2 G(M + M_*)(\Gamma - 1)}{l(l+1)K\Gamma}\right)^{\frac{4}{3}} \times \left(\gamma\left(\frac{3}{4\pi}m_{\rm n}\right)^{\frac{1}{3}}\frac{4\pi\epsilon_0 k_{\rm B}}{e^2}\right)^{4-4\Gamma} A^{\frac{4-4\Gamma}{3}} Z^{8\Gamma-8} T^{4-4\Gamma}. \tag{43}$$

Combining equations (38), (39), (40), and (41) gives an expression for the resonance time in the elastic crust case

$$t_r \sim \frac{1}{4\beta}\left(\left(\frac{p_{\rm o}}{\breve{\mu}}\right)\frac{R_\star^2 m^2 G(M + M_*)(\Gamma - 1)}{l(l+1)K\Gamma}\right)^{\frac{4}{3}} \times \left(\gamma\left(\frac{3}{4\pi}m_{\rm n}\right)^{\frac{1}{3}}\frac{4\pi\epsilon_0 k_{\rm B}}{e^2}\right)^{4-4\Gamma} A^{\frac{4-4\Gamma}{3}} Z^{8\Gamma-8} T^{4-4\Gamma}. \tag{44}$$

These analytical estimates for the mode frequency and resonance time will allow for parameter extraction, should tidal resonances from these modes be observed.

3.4 Ocean mode results

We now discuss the numerical values we choose for model parameters and present the computed mode results.

3.4.1 Neutron star model parameters

Our neutron star model has a central density $\rho_{\rm c} = 10^{15}$ g cm^{-3}. We choose $\Gamma = 2$ as was done by Passamonti et al. (2021). The value of K that we use is $K = 6.67 \times 10^4$ cm^5 g^{-1} s^{-2}. These choices yield a neutron star that has radius $R_\star = 12.5$ km and a mass $M = 1.25$ M$_\odot$. This is just smaller than the peak mass of the Galactic neutron star population 1.39 M$_\odot$ (Antoniadis et al. 2016; Alsing, Silva & Berti 2018). For our computations, we fix the temperature $T = 10^8$ K at the crust–ocean interface, so that $t_r < 100$ yr for all scenarios considered. A longer resonance time would be practically too long for the coincident detection of tidal resonances with compact binary mergers. We note that to get temperatures as hot as $T = 10^8$ K in the crust, one typically needs heating due to accretion (Fujimoto et al. 1984; Haensel & Zdunik 1990, 2003, 2008). For this simple study, we do not account for accretion when computing the tidal wave amplitudes or energies.

The ratio of the ocean floor depth to the neutron star radius is independent of the choice of K in the equation of state. From equation (6), we find that the ocean floor depths of the three oceans are $h_{\rm o,\,c} = 1.14 \times 10^{-4} R_\star$, $h_{\rm o,\,o} = 2.71 \times 10^{-5} R_\star$, and $h_{\rm o,\,i} = 8.03 \times 10^{-8} R_\star$ for carbon, oxygen, and iron, respectively.

The carbon and oxygen oceans form below the electron capture density of those elements, so the bottoms of these oceans would be a dense plasma of ions and electrons (Bildsten & Cutler 1995). For simplicity, we neglect the effect of the ocean having distinct layers and leave this to future work.

3.4.2 Neutron star ocean modes

We solve equation (25) using a four-stage Runge–Kutta scheme. We use a shooting method (Press et al. 1986) to obtain the frequencies of each mode. The unphysical nature of our neutron star model at the surface (i.e. that both $p = 0$ and $\rho = 0$ at $R_\star$) causes a divergence in equation (25). To avoid this divergence, we must choose a coordinate r just below $R_\star$ at which to impose the surface boundary condition equation (27). This ensures that our neutron star ocean model is well behaved throughout the region in which we solve the hydrodynamic equations. Bildsten & Cutler (1995) and Piro & Bildsten (2005a) each address this, with Bildsten & Cutler (1995) choosing to apply the boundary condition at density $\rho = 10^7$ g cm^{-3} and Piro & Bildsten (2005a) choosing to apply the boundary conditions at column depth 10^7 g cm^{-2}. In this work, we apply the surface boundary condition at the radial coordinate corresponding to $p = 0.05 p_{\rm o}$. Our mode frequency calculations are robust in the following sense: applying the surface boundary condition for five different cut-offs ($p = 0.05 p_{\rm o}$, $p = 0.01 p_{\rm o}$, $p = 0.005 p_{\rm o}$, $p = 0.001 p_{\rm o}$, and $p = 0.0001 p_{\rm o}$), we find that the computed mode frequencies change by order unity. Present limitations in the theory of neutron star oceans and atmospheres prevent achieving mode frequency calculations more accurate than within an order of magnitude.

Because tidal forces correspond to $l \geq 2$ spherical harmonics, $l = 0$ and $l = 1$ modes remain practically unaffected by tidal forces, so we do not solve for them. We only solve for $l = 2$ modes as those are the modes most likely to be excited tidally. As previously mentioned, we assume that the neutron star is barotropic so that $\Gamma_1 = \Gamma = 2$. As such, our ocean is unstratified and cannot sustain g modes in the traditional sense (i.e. where the equation of state of the perturbed fluid differs from the background equation of state).

For each ocean model, we find that the ocean can sustain one $l = 2$ mode with a frequency below the orbital frequency at which two neutron stars merge ($\gtrsim 10^3$ Hz; Abbott et al. 2019). As previously mentioned, the modes we find are not the surface g modes found by McDermott et al. (1988) and Passamonti et al. (2021). Instead these modes are interface modes or i modes associated with the crust–ocean interface and ocean surface. These modes resemble shallow ocean surface waves due to the fixed crust–ocean boundary and free ocean surface (Piro & Bildsten 2005a). We note that stratified models can produce g modes with frequencies of order $\sim$1 Hz (Bildsten & Cutler 1995). Table 1 shows the densities at the ocean floor, the depths, and the mode frequencies of the neutron star ocean models, as well as integrals computed later in the paper.

The mode frequency increases with the square root of ocean depth as predicted by equation (35). Carbon oceans have the highest mode frequency at 16.7 Hz, while iron oceans have a mode frequency of 0.44 Hz. We note that the fully computed mode frequencies are each a factor of 2 smaller than the rough estimates obtained from equation (37). To determine the elastic crust i-mode frequencies, we

Table 1. The properties of the three neutron star oceans we consider in this work. We show the atomic number and mass of each element that we consider as the dominant substance in a $T = 10^8$ K neutron star crust as well as the densities at the ocean floors calculated from equation (5), the ocean depths from equation (6), the analytic angular mode frequency from equation (35), the numerically computed angular frequencies and mode frequencies of each ocean, the numerically computed angular frequencies and mode frequencies scaled by $\sqrt{\frac{\bar{\mu}}{p}} = 0.1$ to estimate the crust-penetrating mode frequencies, the dimensionless overlap integrals discussed in Section 4, as well as the integral H_n, defined in Section 5.3, which is related to the quadrupole moment of the mode. The ocean depths, mode frequencies, and integrals are all specific to this choice of equation of state and neutron star core density.

Ocean make-up	Carbon	Oxygen	Iron
Z	6	8	26
A	12	16	56
Melting density at $T = 10^8$ K (g cm^{-3})	1.10×10^{11}	2.71×10^{10}	8.03×10^{7}
Ocean depth h_o ($R_\star$)	1.14×10^{-4}	2.71×10^{-5}	8.03×10^{-8}
Ocean depth h_o when $R_\star = 12.5$ km (cm)	143	33.9	1.01×10^{-1}
Analytic angular frequency ω_i (s^{-1})	241	117	6.40
Numerical angular frequency ω (s^{-1})	104.7	50.98	2.778
Mode frequency f (Hz)	16.66	8.114	0.4422
Crust-penetrating angular frequency ω (s^{-1})	10.47	5.098	0.2778
Crust-penetrating mode frequency f (Hz)	1.666	0.8114	0.044 22
$\tilde{Q}_n$	1.2897×10^{-4}	3.0604×10^{-5}	9.0901×10^{-8}
H_n (g cm^2)	2.738×10^{41}	6.494×10^{40}	1.929×10^{38}

scale our numerically computed frequencies by $\sqrt{\frac{\bar{\mu}}{p_0}} \sim 0.1$ (Piro & Bildsten 2005a), and report these in Table 1 below the rigid crust mode frequencies.

Fig. 1 plots the radial and tangential components of the Lagrangian displacement for the three ocean modes. Each mode exhibits similar structure. The radial component $U(r)$ for each ocean has no nodes and peaks near the middle of the ocean. The tangential component $V(r)$ varies little throughout the three oceans, but well exceeds the radial component throughout.

4 TIDAL INTERACTION

We now reintroduce the potential χ to equation (10), making χ the tidal potential from a nearby companion object. The tidal potential for a companion point mass orbiting in the plane of the neutron star equator takes the form (Press & Teukolsky 1977; Lai 1994)

$$\chi = -\sum_{l=2}^{\infty}\sum_{m=-l}^{l}\frac{GM_* r^l}{D(t)^{l+1}} W_{lm} \mathrm{e}^{-\mathrm{i}m\Phi(t)} Y_{lm}(\theta,\phi), \tag{45}$$

where M_* is the mass of the companion, $D(t)$ is the separation between the two stars as a function of time, $\Phi(t)$ is the true anomaly, and W_{lm} is the numerical coefficient (Press & Teukolsky 1977).

$$W_{lm} = (-1)^{\frac{l+m}{2}} \frac{\left(\left(\frac{4\pi}{2l+1}\right)(l-m)!(l+m)!\right)^{\frac{1}{2}}}{2^l\left(\frac{l-m}{2}\right)!\left(\frac{l+m}{2}\right)!}, \tag{46}$$

where $l + m$ must be even.

Adding the external potential χ to equation (16) and setting $\breve{\mu} = 0$ gives

$$\partial_t^2 \boldsymbol{\xi} + \nabla\delta\tilde{\mu} = -\nabla\chi. \tag{47}$$

Having obtained normal mode solutions to the homogenous equation $\boldsymbol{\xi}_n$, we make an ansatz to solve equation (47) (Lai 1994):

$$\boldsymbol{\xi} = \sum_n a_n(t)\boldsymbol{\xi}_n, \tag{48}$$

where $a(t)$ is an amplitude that scales the eigenfunction and encodes all time dependence of $\boldsymbol{\xi}$. Using the operator $\mathcal{L}\boldsymbol{\xi} = \rho\nabla\delta\tilde{\mu}$ defined in Section 3.1 with $\breve{\mu} = 0$, equation (47) becomes

$$(\rho\partial_t^2 + \mathcal{L})\boldsymbol{\xi} = -\rho\nabla\chi. \tag{49}$$

Substituting our ansatz for $\boldsymbol{\xi}$ gives

$$-\rho\nabla\chi = \sum_n \rho\ddot{a}_n(t)\boldsymbol{\xi}_n + a_n(t)\mathcal{L}\boldsymbol{\xi}_n = \sum_n (\ddot{a}_n(t) + \omega_n^2 a_n(t))\rho\boldsymbol{\xi}_n, \tag{50}$$

where the last equality follows from equation (20). We use the orthogonality condition in equation (21) to isolate an equation for $a_n(t)$. Applying orthogonality yields

$$\ddot{a}_n(t) + \omega_n^2 a_n(t) = -\frac{1}{A_n^2}\int \rho\boldsymbol{\xi}_n^* \cdot \nabla\chi \mathrm{d}V. \tag{51}$$

Inputting the tidal potential from equation (45), equation (51) becomes

$$\ddot{a}_n(t) + \omega_n^2 a_n(t) = \frac{GM_*}{D(t)^{l+1}} W_{lm}\frac{Q_n}{A_n^2}\mathrm{e}^{-\mathrm{i}m\Phi(t)}, \tag{52}$$

where Q_n is the overlap integral defined by (Press & Teukolsky 1977; Lai 1994; Tsang et al. 2012; Tsang 2013; Andersson & Pnigouras 2020; Passamonti et al. 2021)

$$Q_n = \int \rho\boldsymbol{\xi}_n^* \cdot \nabla(r^l Y_{lm}(\theta,\phi))\mathrm{d}V = l\int \rho(U + V(l+1))r^{l+1}\mathrm{d}r, \tag{53}$$

where we have used equation (22) to obtain the last equality. Note that the overlap integral is entirely a property of the mode and quantifies how strongly the mode gets excited by tidal forces. We define a normalized overlap integral, dimensionless for the $l = 2$ modes, as

$$\tilde{Q}_n = \frac{Q_n}{A_n^2}. \tag{54}$$

In Table 1, we report the normalized overlap integrals for each of the three ocean modes. We must also estimate the overlap integrals for modes that penetrate into the elastic crust. Piro & Bildsten (2005a) determined that the mode energy is principally confined to the ocean, even when the mode penetrates into the crust. Furthermore, while the radial displacement has a node in the ocean with an elastic crust

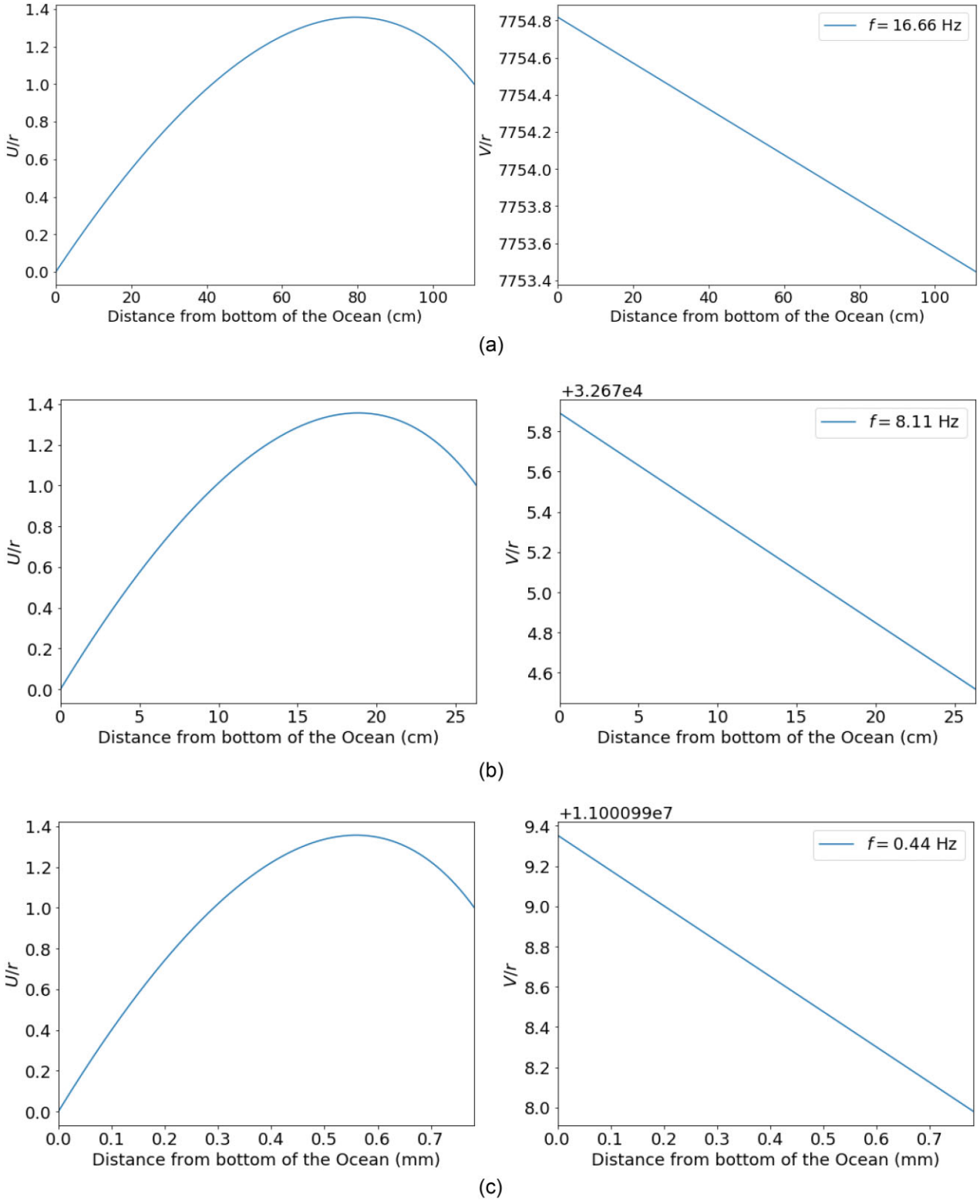

Figure 1. The shallow ocean surface mode for the three neutron star ocean models we study in this paper: (a) the carbon ocean, (b) the oxygen ocean, and (c) the iron ocean. The left-hand plots show the dimensionless function $\frac{U(r)}{r}$ as a function of distance from the ocean floor, while the right-hand plots show the dimensionless function $\frac{V(r)}{r}$ as a function of distance from the ocean floor. Note that horizontal axis in (c) is in mm because the iron ocean is only 1 mm deep. The mode frequency of each ocean model is shown in the legend of the right-hand plot.

and not with a rigid crust, the tangential displacement of Piro & Bildsten (2005a) is multiple orders of magnitude larger than the radial displacement. Because our computed rigid crust modes have this same property, the large tangential displacement in the ocean

will dominate the overlap integral in both cases. Consequently, we use our computed rigid crust overlap integrals to estimate the overlap integrals of i modes that penetrate into the crust.

Following the analysis of Lai (1994), we perform a change of variables to solve equation (52) where

$$a(t) = GM_*\tilde{Q}_n W_{lm} b(t) \mathrm{e}^{-\mathrm{i}m\Phi(t)}, \tag{55}$$

and $b(t)$ is the new function to solve for. In terms of $b(t)$, equation (52) becomes

$$\ddot{b} - 2\mathrm{i}m\dot{\Phi}\dot{b} + (\omega^2 - m^2\dot{\Phi}^2 - \mathrm{i}m\ddot{\Phi})b = \frac{1}{D(t)^{l+1}}. \tag{56}$$

If we decompose b into a real part b^{r} and an imaginary part b^{i}, equation (56) becomes the following two equations:

$$\ddot{b}^{\mathrm{r}} + 2m\dot{\Phi}\dot{b}^{\mathrm{i}} + m\ddot{\Phi}b^{\mathrm{i}} + (\omega^2 - m^2\dot{\Phi}^2)b^{\mathrm{r}} = \frac{1}{D(t)^{l+1}}, \tag{57a}$$

$$\ddot{b}^{\mathrm{i}} - 2m\dot{\Phi}\dot{b}^{\mathrm{r}} - m\ddot{\Phi}b^{\mathrm{r}} + (\omega^2 - m^2\dot{\Phi}^2)b^{\mathrm{i}} = 0. \tag{57b}$$

Given an orbital trajectory for a companion celestial body, equations (57a) and (57b) can be solved. By plugging solutions to equations (57a) and (57b) back into equation (55), the tidal wave amplitude $a(t)$ in the neutron star ocean can be found.

4.1 Tidal interaction scenarios

We consider three tidal interaction scenarios: a binary neutron star (BNS) inspiral in a circular orbit, a neutron star–black hole (NSBH) binary inspiral in a circular orbit, and an unbound parabolic encounter between two neutron stars (NSPE). While NSPEs are expected to be fairly rare (Tsang 2013) due to the low presence of neutron stars predicted in stellar clusters (Bae, Kim & Lee 2014; Belczynski et al. 2018; Ye et al. 2020; Mandel & Broekgaarden 2022), tidal interactions from these events remain relatively unexplored beyond Tsang (2013), so we consider them in this work. In the following sections, we enumerate the initial conditions and orbital parameters in each of these scenarios.

4.1.1 Neutron star binary and neutron star–black hole binary

The initial conditions and orbital motion of BNSs and NSBHs are largely the same when the orbital separation well exceeds the diameter of stellar-mass black holes. Due to the lower mode frequencies of the three neutron star oceans, resonance will occur earlier in the inspiral than f-mode resonances. As such, we consider both BNSs and NSBHs at earlier times.

For an inspiraling circular binary, the time derivative of the true anomaly $\dot{\Phi}$ is just the orbital frequency

$$\dot{\Phi} = \sqrt{\frac{G(M + M_*)}{D(t)^3}}, \tag{58}$$

where G is the gravitational constant, M is the mass of the neutron star that is tidally perturbed, M_* is the mass of the companion object, and $D(t)$ is the orbital separation as a function of time. The second derivative of the true anomaly is

$$\ddot{\Phi} = -\frac{3}{2}\dot{\Phi}\frac{\dot{D}}{D}, \tag{59}$$

where $\dot{D}$ is the time derivative of D. Due to the emission of GWs, the binary loses energy and $D(t)$ decreases over time. The separation as a function of time $D(t)$ for an inspiraling circular binary is given by (Peters 1964)

$$D(t) = \left(D_0^4 - \frac{256}{5}\frac{G^3 M M_*(M + M_*)}{c^5}t\right)^{1/4}, \tag{60}$$

where D_0 is the orbital separation at time $t = 0$, and c is the speed of light. We have neglected the effects of energy transfer to the neutron star ocean on the orbital motion because, as will be discussed in Section 4.2.3, the orbital energy will far exceed the energy transmitted to the ocean mode.

To numerically solve equations (57a) and (57b), we must choose initial values for b^{r}, b^{i}, $\dot{b}^{\mathrm{r}}$, and $\dot{b}^{\mathrm{i}}$. We use the same initial conditions for circular binary inspirals used by Lai (1994) and start our integration at a time when the binary is very far from merging. These conditions are

$$b^{\mathrm{r}}(0) = \frac{1}{D^{l+1}(\omega^2 - m^2\dot{\Phi}^2)}, \tag{61a}$$

$$\dot{b}^{\mathrm{r}}(0) = \left[-(l+1)\frac{\dot{D}}{D} + \frac{2m^2\dot{\Phi}\ddot{\Phi}}{\omega^2 - m^2\dot{\Phi}}\right] b^{\mathrm{r}}(0), \tag{61b}$$

$$b^{\mathrm{i}}(0) = \frac{1}{(\omega^2 - m^2\dot{\Phi})}(2m\dot{\Phi}\dot{b}^{\mathrm{r}}(0) + m\ddot{\Phi}b^{\mathrm{r}}(0)), \tag{61c}$$

$$\dot{b}^{\mathrm{i}}(0) \approx 0. \tag{61d}$$

We compute b for the $l = 2$, $m = 2$ cases, since $m = 2$ and $m = -2$ modes will be equally excited (Lai 1994). The $m = 0$ binary inspiral cases will be small compared to the $m = 2$ resonant case. The $m = 0$ case corresponds to static deformations of the neutron star, rather than the larger amplitude resonant oscillations. Resonance of the ocean mode with the tidal force is likely to occur in any isolated binary system containing a neutron star because the system's orbital frequency continuously evolves. We do not compute the $m = \pm 1$ case since $Y_{2\pm1} = 0$.

4.1.2 Neutron star parabolic encounter

We consider close encounters of neutron stars whose minimum distance of approach is a distance s. Since parabolic orbits correspond to those with an orbital eccentricity of $e = 1$, the orbital separation as a function of radius is

$$D(t) = \frac{2s}{1 + \cos\Phi(t)}, \tag{62}$$

where $\Phi(t)$ here is the true anomaly for a parabolic orbit. Using conservation of angular momentum, we obtain a differential equation for the true anomaly as a function of time:

$$\dot{\Phi}(t) = \frac{1}{4}\sqrt{\frac{G(M + M_*)}{s^3}}(1 + \cos\Phi(t))^2. \tag{63}$$

We also obtain the second derivative of the true anomaly $\ddot{\Phi}$ by taking the derivative of $\dot{\Phi}$:

$$\ddot{\Phi}(t) = -\frac{1}{2}\sqrt{\frac{G(M + M_*)}{s^3}}(1 + \cos\Phi(t))\sin\Phi(t)\dot{\Phi}(t). \tag{64}$$

Solving equation (63) gives the true anomaly as a function of time for a parabolic orbit.

Again, we must choose appropriate initial conditions for b^{r}, b^{i}, $\dot{b}^{\mathrm{r}}$, and $\dot{b}^{\mathrm{i}}$ to solve equations (57a) and (57b). For a parabolic orbit, the two bodies begin infinitely far away from one another with no speed. Thus, when the companion object is far away from the neutron star, we have $\dot{\Phi}(t) \approx 0$ and $\ddot{\Phi}(t) \approx 0$. When this is the case, $D(t)$ is

approximately constant, so we obtain a first approximation to b at large distances:

$$b \approx \frac{1}{\omega^2 D(t)^{l+1}}. \tag{65}$$

The time derivative $\dot{b}$ becomes

$$\dot{b} \approx -(l+1)\frac{\dot{D}(t)}{D(t)}b, \tag{66}$$

where $\dot{D}(t)$ is the time derivative of orbital separation. Taking the time derivative of equation (66) gives

$$\ddot{b} \approx \left(-(l+1)\frac{\ddot{D}}{D} + (l+2)(l+1)\left(\frac{\dot{D}}{D}\right)^2\right)b, \tag{67}$$

where $\ddot{D}$ is the second time derivative of orbital separation. We may plug equations (66) and (67) into equation (56) and obtain an expression for b containing initial conditions for both $b^{\rm r}$ and $b^{\rm i}$:

$$b \approx \frac{1}{D^{l+1}}\frac{\omega^2 - m^2\dot{\Phi}^2 + {\rm i}(m\ddot{\Phi} - 2m(l+1)\dot{\Phi}\frac{\dot{D}}{D})}{\omega^4}, \tag{68}$$

where we have kept only the largest terms. Separating equation (68) into a real and an imaginary part, we get initial conditions valid when $D(t) >> s$

$$b^{\rm r}(0) = \frac{1}{\omega^2 D^{l+1}}, \tag{69a}$$

$$\dot{b}^{\rm r}(0) = -(l+1)\frac{\dot{D}}{D}b^{\rm r}(0), \tag{69b}$$

$$b^{\rm i}(0) = \frac{1}{\omega^2}(2m\dot{\Phi}\dot{b}^{\rm r}(0) + m\ddot{\Phi}b^{\rm r}(0)), \tag{69c}$$

$$\dot{b}^{\rm i}(0) \approx 0. \tag{69d}$$

We solve for b in the cases where $l = 2$ and $m = 0$. The $m = 2$ NSPE tidal amplitude will be significantly weaker than the $m = 0$ amplitude as resonant oscillations during NSPEs require very specific initial conditions on the neutron star trajectories, making them less likely to be found in nature.

4.2 Tidal results

We report our results for the BNS, NSBH, and NSPE cases. $a(t)$ is computed by numerically solving equations (57a) and (57b) for $b(t)$ and substituting $b(t)$ into equation (55). The companion mass used in the BNS and NSPE is 1.25 $M_\odot$ and the companion mass used in the NSBH is 20 $M_\odot$. We show results for the NSPE when $m = 0$ and the binary inspirals when $m = 2$. We report one tidal response for each possible combination of ocean and companion orbit. Table 2 contains the main quantitative results of this paper.

4.2.1 Resonant tidal waves in binary inspirals

Both BNS and NSBH inspirals will resonantly excite the ocean modes of their component neutron stars. It is when resonance occurs that the tidal wave achieves its maximum amplitude.

In Fig. 2, we show the magnitude of the tidal wave amplitudes for both BNSs and NSBHs in the times surrounding resonance.

The general evolution of the tidal amplitudes of all three oceans is similar between both BNSs and NSBHs. In the minutes leading up to resonance, the amplitudes of the tidal waves increase by a full order of magnitude. We have not considered any damping mechanisms, although possible mechanisms that can decrease the tidal wave amplitudes include diffusion (Dommes & Gusakov 2021; Kraav, Gusakov & Kantor 2021), heating (Beloborodov & Li 2016), and GW emission (Lioutas & Stergioulas 2018). Without damping, the tidal wave continues to pulsate with the same amplitude following the resonance time. Carbon and oxygen oceans possess tidal wave amplitudes of similar size. The overlap integrals and mode frequencies of these modes are less than an order of magnitude different, with carbon oceans having larger amplitudes. In contrast, the amplitudes in the iron ocean are about a factor of 100 less than those in the oxygen ocean. These differences result from the different overlap integrals calculated for each ocean.

Slight differences between the BNS and the NSBH cases are apparent. The BNS cases generate higher amplitudes than the NSBH cases because resonance during a BNS occurs when the two bodies are roughly twice as close as during an NSBH. Additionally, the evolution of the tidal wave amplitude and frequency is noticeably slower in the BNS cases. This is a direct consequence of the slower frequency evolution in BNSs.

We determine how long before merger these resonances occur from equation (60). We make D_0 the separation at resonance time, set $D(t) = 0$, and solve for t. In BNSs with rigid crusts, the carbon ocean reaches resonance with the tidal force ∼5 min before merger, the oxygen ocean reaches resonance ∼40 min before merger, and the iron ocean reaches resonance ∼60 d before merger. When scaling these results for elastic crusts, the carbon ocean reaches resonance ∼40 h before merger, the oxygen ocean reaches resonance ∼10 d before merger, and the iron ocean reaches resonance ∼70 yr before merger. In NSBHs with rigid crusts, the carbon ocean reaches resonance ∼1 min before merger, the oxygen ocean reaches resonance ∼5 min before merger, and the iron ocean reaches resonance ∼7 d before merger. Scaling these results for elastic crusts gives resonance times ∼5 h before merger in carbon oceans, ∼30 h before merger in oxygen oceans, and ∼10 yr before merger in iron oceans. Thus, any emission from the tidally resonant oceans would well precede corresponding compact binary mergers.

4.2.2 Tidal waves excited by parabolic encounters

NSPEs will excite tidal waves in neutron star oceans at periastron. When this occurs, the tidal force of the companion star provides an impulse to the ocean, causing it to pulsate. In this paper, we quote results when the closest distance of approach is $s = 3.4 \times 10^6$ cm. This is the distance of closest approach where the carbon ocean tidal wave amplitude $a(t)$ in an NSPE is approximately equal to that of a BNS. For different values of s, the amplitudes of the excited tidal waves will scale our results by a factor of $(s/3.4 \times 10^6\ {\rm cm})^{-3}$. Fig. 3 shows the tidal wave amplitudes during an NSPE for the three oceans.

After the NSPE occurs, the tidal waves will oscillate with the mode frequency of the ocean mode. The amplitudes are approximately the same order for each of the three oceans we consider. As in the binary inspiral cases, the iron ocean has the smallest amplitude. The distance of closest approach in this NSPE is about an order of magnitude smaller than the resonance distance in the binary inspiral case. NSPEs require closer encounters than NSBHs and BNSs to produce sizable ocean tidal waves.

We estimate the event rate for NSPEs within this nominal encounter distance inside a globular cluster. NSPE event rates have been computed in previous works (Kocsis, Gáspár & Márka 2006; Tsang 2013), but not for these very small encounter distances. We

Table 2. The main quantitative results of this paper for the three neutron star oceans and three tidal scenarios considered. This table includes the energy deposited into each ocean due to the tide and the time at which this energy is deposited. The energy reported for the NSPE corresponds to $s = 3.4 \times 10^6$ cm.

Ocean	Carbon (rigid)	Oxygen (rigid)	Iron (rigid)	Carbon (elastic)	Oxygen (elastic)	Iron (elastic)
Energy deposited (erg)	8.6×10^{46}	3.8×10^{45}	1.3×10^{40}	8.6×10^{44}	3.8×10^{43}	1.3×10^{38}
Time before BNS merger (min)	5.33	35.33	8.3×10^4	2.5×10^3	1.6×10^4	3.9×10^7
Energy deposited in NSBH (erg)	3.9×10^{46}	1.7×10^{45}	5.8×10^{39}	3.9×10^{44}	1.7×10^{43}	5.8×10^{37}
Time before NSBH merger (min)	0.67	4.5	1.1×10^4	310	2.1×10^3	4.9×10^6
Energy deposited in NSPE (erg)	4.3×10^{46}	2.5×10^{45}	2.3×10^{40}	4.3×10^{44}	2.5×10^{43}	2.3×10^{38}
Time before NSPE (s)	0	0	0	0	0	0

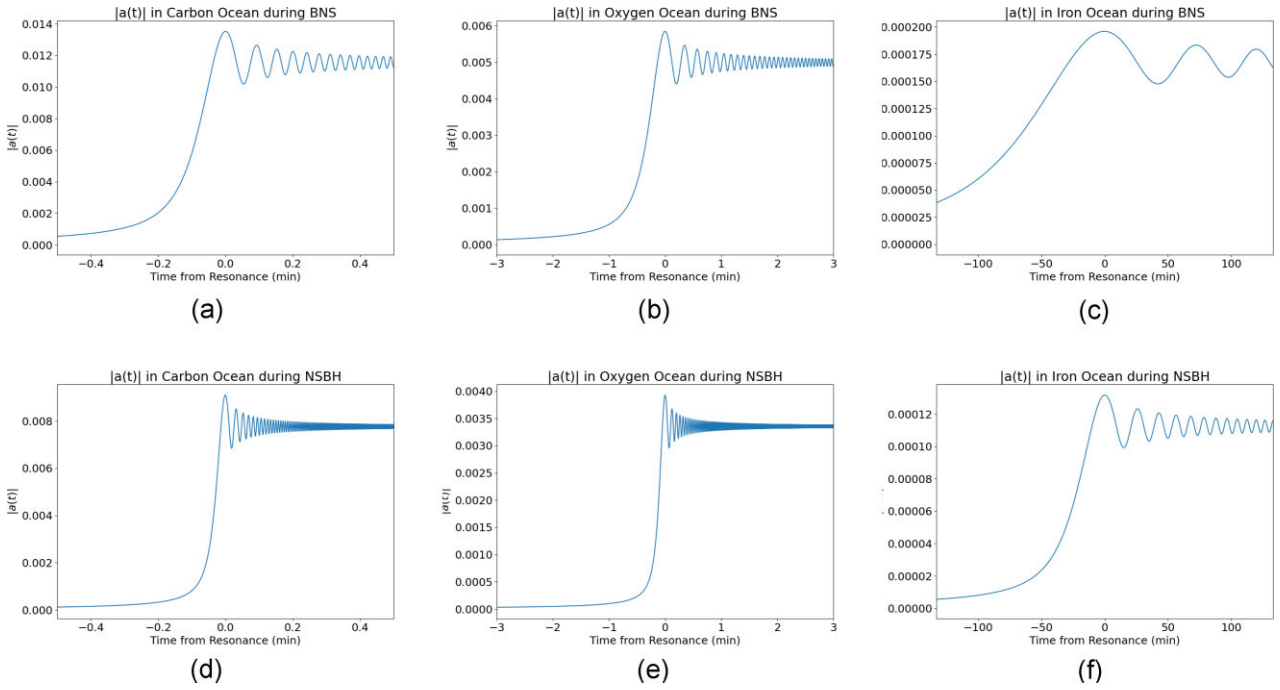

Figure 2. The magnitudes of the dimensionless resonant ocean tidal wave amplitude $|a(t)|$ during compact binary inspirals as a function of time without damping. The horizontal axis shows the time from resonance in hours and the vertical axis shows $|a(t)|$. The top row shows tidal wave amplitudes during a BNS (a) in a carbon ocean, (b) in an oxygen ocean, and (c) in an iron ocean. The bottom row shows tidal wave amplitudes during an NSBH (d) in a carbon ocean, (e) in an oxygen ocean, and (f) in an iron ocean.

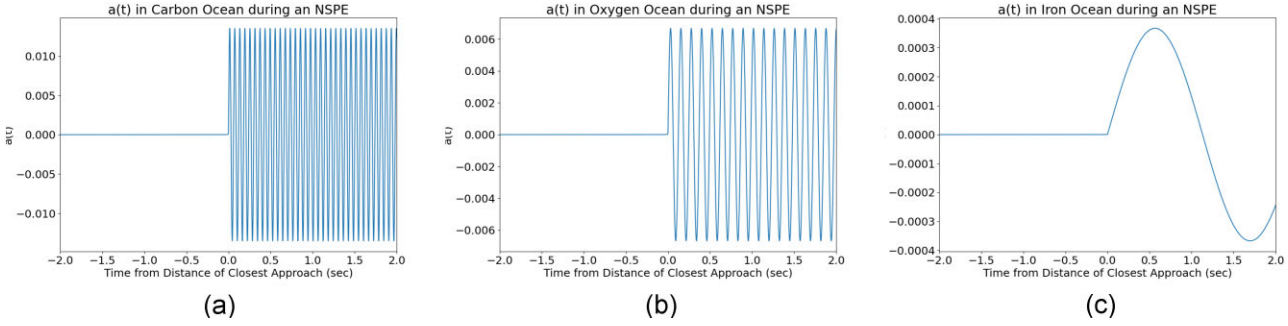

Figure 3. The real part of the dimensionless ocean tidal wave amplitude $a(t)$ during an NSPE as a function of time without damping. The horizontal axis shows the time from resonance in seconds and the vertical axis shows $a(t)$. The sharp increase in the tidal wave height at time $t = 0$ is due to the impulse from the neutron stars reaching their smallest orbital separation. (a) shows tidal wave amplitudes in a carbon ocean, (b) shows the tidal wave amplitude in an oxygen ocean, and (c) shows the tidal wave amplitude in an iron ocean.

estimate the event rate of NSPEs in a globular cluster as

$$\nu_{\rm PE} = \frac{1}{2} N n_\star v_0 \sigma_{\rm PE}, \tag{70}$$

where N is the number of neutron stars in a globular cluster, $n_\star$ is the number density of neutron stars in a globular cluster, $v_0 = \sqrt{\frac{G(M+M_*)}{s}}$ is the relative speed of neutron stars in an NSPE at peri-

astron, and $\sigma_{\rm PE}$ is the cross-section of NSPEs. Note that in this expression for event rate, we use the relative velocity between neutron stars at periastron, while Kocsis et al. (2006) use the relative velocity at infinite separation v_∞. We use the velocity at periastron because we are considering parabolic orbits where $v_\infty = 0$. The cross-section will be

$$\sigma_{\rm PE} = \pi s^2, \tag{71}$$

for the encounter distance s. The event rate for NSPEs within a distance s becomes

$$\nu_{\rm PE} = \frac{1}{2}\frac{N^2}{\frac{4}{3}\pi R_{\rm GC}^3}\sqrt{G(M+M_*)s^3}, \tag{72}$$

where we have assumed that the number density of neutron stars in a globular cluster is uniform such that $n_\star = \frac{N}{\frac{4}{3}\pi R_{\rm GC}^3}$ with $R_{\rm GC}$ being the radius of the globular cluster. Using $N = 500$, $R_{\rm GC} = 1$ pc as was done by Kocsis et al. (2006), and $M = M_* = 1.25\ {\rm M}_\odot$, we find $\nu_{\rm PE} = 5.5 \times 10^{-21}\ {\rm yr}^{-1}$. Close NSPEs are therefore extremely rare.

Despite the rarity of these events, their tidal waves are generated in exact coincidence with the time of the closest passage of the neutron stars, so observation of emission from such tides can exactly demarcate the time of periastron.

4.2.3 *Energetics of ocean tidal waves*

The energy of an oscillation mode is divided into potential energy and kinetic energy. The kinetic energy and potential energy are (Lai 1994)

$$E_{\rm k} = \frac{1}{2}\int \rho \frac{\partial \boldsymbol{\xi}}{\partial t}\cdot\frac{\partial \boldsymbol{\xi}^*}{\partial t}{\rm d}V = \frac{1}{2}|\dot{a}(t)|^2 A_n^2, \tag{73a}$$

$$E_{\rm p} = \frac{1}{2}\int \rho\omega_n^2 \boldsymbol{\xi}\cdot\boldsymbol{\xi}^*{\rm d}V = \frac{1}{2}\omega_n^2|a(t)|^2 A_n^2. \tag{73b}$$

After tidal resonance in binary inspirals, the maximum kinetic and potential energies should be equal. Additionally, both the $m = 2$ and $m = -2$ modes contribute to the energy equally. Therefore, the tidal interaction will deposit a total energy into each mode (Lai 1994):

$$E = \omega_n^2|a_{n,\max}|^2 A_n^2, \tag{74}$$

where $|a_{n,\max}|$ is the maximum amplitude of the tidal wave. For the NSPE $m = 0$ case, only one mode contributes to the deposited energy. The NSPE total energy will be half of the energy of a binary inspiral of the same amplitude (Lai 1994).

We compute the energy deposited into the shallow ocean surface mode after tidal resonance during a BNS inspiral to be $\sim 8.6 \times 10^{46}$ erg in a carbon ocean, $\sim 3.8 \times 10^{45}$ erg in an oxygen ocean, and $\sim 1.3 \times 10^{40}$ erg in an iron ocean. Similarly, we compute the energy deposited into the ocean after tidal resonance during an NSBH inspiral to be $\sim 3.9 \times 10^{46}$ erg in a carbon ocean, $\sim 1.7 \times 10^{45}$ erg in an oxygen ocean, and 5.8×10^{39} erg in an iron ocean. The orbital energy at the time of resonance is $\gtrsim 10^{50}$ erg, justifying our assumption that the orbital motion remains unaffected.

After an NSPE whose distance of closest approach is $s = 3.4 \times 10^6$ cm, we compute the energy deposited into the shallow ocean surface mode to be 4.3×10^{46} erg for carbon oceans, 2.5×10^{45} erg for oxygen oceans, and 2.3×10^{40} erg for iron oceans. For different values of s, these energy results will scale by $(s/3.4 \times 10^6\ {\rm cm})^{-6}$.

The mode energy has dependence $E \propto \omega_n^2 Q_n^2$. Because the mode frequency in the elastic case is the shallow ocean surface mode frequency scaled by $\sqrt{\frac{\tilde{\mu}}{p}}$, the energy deposited into the crust-penetrating i modes should be the energy deposited into the corresponding shallow ocean surface modes scaled by a factor of $\frac{\tilde{\mu}}{p} \sim 0.01$ (Piro & Bildsten 2005a). Consequently, our energy results for the elastic crust cases are the energies reported above, reduced by a factor of 100. We also report these values in Table 1.

5 DISCUSSION

We have determined that tidal waves in neutron star oceans can be generated during BNS inspirals, NSBH inspirals, and NSPEs, and quantitatively estimated their amplitudes, energies, and timing. The tidal waves in each of these systems have unique properties. In binary inspirals, the neutron star ocean mode becomes resonant with the tidal force of the companion minutes to days before coalescence if the crust is rigid, and hours to years if the crust is elastic. Conversely, the impulsive tidal force during an NSPE excites the ocean mode at the moment of closest approach. The impulse generates simple continuous oscillatory tidal waves with the frequency of the neutron star ocean mode. The implications of these results extend to multimessenger astronomy and neutron star geophysics.

5.1 Ocean tidal waves as compact binary merger precursor flares and parabolic encounter multimessenger sources

Dynamical activity in neutron star oceans may emit neutrino and electromagnetic radiation (Reisenegger & Goldreich 1994; Heyl 2004; Deibel 2016; Wang et al. 2021). Additionally, mode oscillations have been observed during electromagnetic bursts (Strohmayer & Mahmoodifar 2014). Therefore, the tidal waves in neutron star oceans during a binary inspiral might correspond to multimessenger emission. We hypothesize that tidally resonant ocean waves in neutron stars may be a new source of compact binary merger precursor emission.

The energies deposited into the ocean modes after resonance (computed in Section 4.2.3) represent estimates of the energy available for these flares. Thus, $\sim 10^{37}-10^{46}$ erg are available to source tidally resonant ocean flares. The energy deposited into the carbon and oxygen oceans during NSBHs and BNSs is comparable to the breaking energy of neutron star crusts, which ranges from 10^{44} to 10^{46} erg (Tsang et al. 2012; Baiko & Chugunov 2018). Consequently, the energy imparted to the ocean may affect the neutron star crust. If the deposited energy exceeds the breaking energy, the crust may either crack or melt. Past work on crust breaking by resonant i modes has mostly focused on the crust–core i mode (Tsang et al. 2012; Passamonti et al. 2021). Our results show that the crust–ocean i mode may have the ability to break the crust from the top, leading to interesting physics within the ocean. Additionally, while we have neglected the presence of magnetic fields, the interaction between the excited ocean and the surface magnetic field could generate electromagnetic emission. Particularly, if the neutron star crust breaks, subsequent magnetic reconnection of the surface magnetic field may cause large electromagnetic flares (Lander et al. 2015; Kaspi & Beloborodov 2017, for example). Because neutron star surfaces also emit thermal neutrinos (Yakovlev & Pethick 2004, for example), it is possible that this emission is manifested in neutrinos. In the remainder of this paper, we will limit our discussion to accompanying electromagnetic emission.

Pre-existing mechanisms for producing compact binary merger precursor flares include interactions of neutron star magnetospheres in BNSs (Ascenzi et al. 2021), orbital motion of a weakly magnetized companion and a highly magnetized neutron star in either BNSs or NSBHs (Vietri 1996; Hansen & Lyutikov 2001; McWilliams & Levin 2011; Lai 2012; Piro 2012; Sridhar et al. 2021), and tidally induced cracking of a neutron star crust during high-frequency mode tidal

resonances in either BNSs or NSBHs (Gittins et al. 2020; Suvorov & Kokkotas 2020; Kuan, Suvorov & Kokkotas 2021a; Passamonti et al. 2021). Precursor flares from previously considered channels are only expected just before a merger ($\lesssim$10 s; Mathews & Wilson 1997; Passamonti et al. 2021; Sridhar et al. 2021).

In contrast to these other mechanisms, precursor flares associated with tidally resonant neutron star ocean waves could be excited minutes to even years before the merger. Tidally resonant ocean flares can therefore be early warning signs of compact binary mergers involving neutron stars. Notably, NSBHs should have less trouble emitting early flares since the black hole will be farther from the neutron star than in other scenarios and should not absorb all the emission.

Early warning precursor flares can be additional messengers for studying neutron stars and compact binary systems. The time before merger will provide information about both the types of merger and the material in neutron star oceans. In fact, the delay between flare and merger can distinguish these qualities. Simply observing a flare within 100 yr of a corresponding merger significantly constrains the parameter space and provides limits on the crust temperature. Because a crust temperature of $T \sim 10^8$ K is needed to ensure that all our considered scenarios have resonance times of less than 100 yr, a successful flare observation could suggest a higher crust temperature and consequently provide information about surface heating and accretion during compact binary inspirals.

Observing these flares in practice will likely require retroactive searches for electromagnetic data coincident in sky localization with compact binary mergers observed by GW detectors. The use of space-based GW detectors such as *LISA* (Amaro-Seoane et al. 2017) may assist in identifying flares in advance of mergers, as space-based detectors will detect GWs from compact binary inspirals well before mergers at galactic distances [Laser Interferometer Space Antenna (LISA) Study Team 2000; Robson, Cornish & Liu 2019]. Observations of tidally resonant ocean flares during compact binary inspirals would complement multimessenger efforts to study these exotic systems and their oceans.

NSPEs could generate flares as well. The ignition of the tidal wave would precisely coincide with the NSPE. As such, coincident detections of the broad-band GW bursts generated by the orbital motion (Turner 1977a; Kovacs & Thorne 1978; Kocsis et al. 2006; De Vittori, Jetzer & Klein 2012) and tidally induced electromagnetic flares can allow for the multimessenger study of NSPEs and their constituent neutron stars.

5.2 Detection of electromagnetic flares from neutron star ocean tidal waves

We posit two possible scenarios for electromagnetic flares originating from neutron star ocean tidal waves and qualitatively discuss their detection. Since the mode frequencies of the oceans studied are $\sim$1−100 Hz, the electromagnetic radiation from neutron star ocean tides may be ultra-low frequency. As of this paper's writing, detection of ultra-low-frequency electromagnetic radiation on geophysical scales has been considered (Grimm 2002; Grimm et al. 2009; Kozakiewicz et al. 2016), but no astronomical electromagnetic instrument capable of tapping frequencies below $\sim$0.001 MHz has been proposed (Bergman et al. 2009; Saks et al. 2010; Blott et al. 2013; Boonstra et al. 2016; Rajan et al. 2016; Belov et al. 2018; Cecconi et al. 2018; Prinsloo et al. 2018; Bentum et al. 2020). Therefore, it would be extremely difficult to detect $\lesssim$100 Hz radiation from neutron star ocean tidal waves.

However, due to complicated microphysics, the large amount of energy deposited into the neutron star ocean, and the potential for magnetic reconnection, we propose that neutron star ocean tides may produce high-energy electromagnetic radiation in the gamma-ray or X-ray regime with spectra and time-scales similar to that of soft-gamma repeaters or type I X-ray bursts, perhaps through interactions between the surface magnetic field and the ocean. The hot temperatures of neutron star surfaces make thermal X-rays a particularly compelling manifestation of this emission. Since we have considered neutron stars with $T = 10^8$ K at the crust, these neutron stars may already be accreting and emitting X-rays thermally. The tidal resonance will impart additional energy into the ocean, which we suppose may increase the flux of photons on time-scales comparable to the period of the computed ocean mode. We note that accretion often requires a non-compact companion to supply material. We have neglected the effects of such additional companions for simplicity.

Taking our high-energy flare conjecture at face-value and assuming that the energy deposited into the ocean from the tide is isotropically expelled as either gamma-rays or X-rays, we estimate how far away a resonant neutron star ocean tidal flare can be detected by the gamma-ray detector *Fermi* (Atwood et al. 2009) and X-ray telescopic array *NuSTAR* (Harrison et al. 2013).

We estimate the photon flux from such a flare by assuming that all energy deposited into the mode is radiated away as either X-rays or gamma-rays. Taking R to be the distance between a detector and the source, we approximate the photon flux at the detector as

$$F_\gamma \approx \frac{E}{E_\gamma}\frac{\omega}{4\pi R^2}, \tag{75}$$

where E is the energy of the ocean tidal wave, E_γ is the energy of a photon, and ω is the mode frequency. We have assumed that all energy is radiated on a time-scale comparable to the inverse of the mode frequency ω as it is the only short time-scale we have.

For *Fermi*, we estimate the furthest distance at which such a flare could be observed as

$$R \approx \sqrt{\frac{E}{E_\gamma}\frac{\omega}{4\pi F_t}}, \tag{76}$$

where F_t is the photon flux threshold for *Fermi*. The photon flux threshold of *Fermi* is 0.74 photons cm^{-2} s^{-1} in the range of 8 keV–40 MeV (Atwood et al. 2009).

For short-duration X-ray sources, *NuSTAR*'s sensitivity is limited by photon statistics. The signal-to-noise ratio (SNR) for a short-duration flare assuming that all photons are at the same energy is

$$K = \sqrt{F_\gamma T \mathcal{A}}, \tag{77}$$

where T is the duration of the flare and $\mathcal{A}$ is the effective area of *NuSTAR*. Substituting our estimate for F_γ and taking $T \approx \omega^{-1}$ gives

$$K \approx \sqrt{\frac{E}{E_\gamma}\frac{\mathcal{A}}{4\pi R^2}}. \tag{78}$$

We estimate the furthest distance at which a flare can be observed by *NuSTAR* as

$$R \approx \frac{1}{K}\sqrt{\frac{E}{E_\gamma}\frac{\mathcal{A}}{4\pi}}, \tag{79}$$

for some SNR threshold K. Notice that ω has dropped out of equation (79), so this estimate is independent of the precise time-scale of the flare as long as it is of short duration (Harrison et al. 2013). The effective area of *NuSTAR* is approximately 800 cm^2 for photon

energies of 6−10 keV and 300 cm^2 for photon energies of 10−30 keV (Harrison et al. 2013). We set a putative SNR threshold of $K = 5$.

We compute the distances for each ocean and binary inspiral case under four detection scenarios: tidally resonant ocean flare photons are (1) gamma-rays with $E_\gamma = 40$ MeV detected by *Fermi*, (2) X-rays with $E_\gamma = 8$ keV detected by *Fermi*, (3) higher energy X-rays with $E_\gamma = 20$ keV detected by *NuSTAR*, and (4) lower energy X-rays with $E_\gamma = 8$ keV detected by *NuSTAR*. Note that $R \propto E^{\frac{1}{2}}$ for both *Fermi* and *NuSTAR* detections. Since the elastic crust energy estimates are the rigid crust energy scaled by $\frac{\mu}{p_o}$, we scale the distances from their rigid crust values by a factor of $(\frac{\mu}{p_o})^{\frac{1}{2}} \sim 0.1$ to extrapolate the distance results for elastic crust case. We quote our results in Table 3.

We find that if the emission from tidally resonant ocean flares is in the gamma-ray spectrum or if crusts are composed of iron, *Fermi* and *NuSTAR* will have almost no capability to detect flares of extragalactic compact binaries, the main sources of interest for ground-based GW detectors. Excitingly, however, if tidally resonant ocean flares are emitted in the X-ray spectrum in carbon or oxygen oceans, both *NuSTAR* and *Fermi* will have the ability to detect them out to distances of the orders of ∼10−1000 Mpc for rigid crusts and even ∼1−100 Mpc for elastic crusts. These distances coincide with the BNS ranges of currently operational GW detectors (LIGO Scientific Collaboration, Virgo Collaboration & KAGRA Collaboration 2021a). In fact, BNS and NSBH inspirals have been observed out to a few 100 Mpc (LIGO Scientific Collaboration & Virgo Collaboration 2019, 2021; LIGO Scientific Collaboration, Virgo Collaboration & KAGRA Collaboration 2021a).

We estimate an optimistic event rate for these flares using the merger rates of BNSs and NSBHs from LIGO–Virgo–KAGRA's third GW catalogue (LIGO Scientific Collaboration, Virgo Collaboration & KAGRA Collaboration 2021b). The 90 per cent credible interval for the merger rates is reported as 10−1700 Gpc^{-3} yr^{-1} for BNSs and 7.8−140 Gpc^{-3} yr^{-1} for NSBHs (LIGO Scientific Collaboration, Virgo Collaboration & KAGRA Collaboration 2021b; Mandel & Broekgaarden 2022). Assuming a flare detectable out to ∼1−100 Mpc, we estimate the event rates for detectable tidally resonant ocean flares by multiplying spherical volumes with radii 1 and 100 Mpc by the lower and upper limits on the quoted merger rates, respectively. The event rates would be $\sim 4 \times 10^{-8}$−7 yr^{-1} for BNSs and $\sim 3 \times 10^{-8}$−0.6 yr^{-1} for NSBHs. Depending on the details of the crust, ocean, and flare, precursor flares associated with tidally resonant ocean waves in compact binary inspirals may be detectable.

5.3 Gravitational waves from neutron star ocean tidal waves

The time-dependent mass density perturbations of tidal pulsations in compact stars should also generate GWs (Turner 1977b). We now investigate the GWs produced by neutron star ocean tidal waves. The GW metric $h_{ij}^{\rm TT}$ (not to be confused with the ocean depth h_o) can be written as a multipole expansion (Turner 1977b):

$$h_{ij}^{\rm TT} = \frac{G}{Rc^4} \sum_{l,m} B_{lm}\left(t - \frac{R}{c}\right) T_{ij}^{lm}(\theta, \phi), \tag{80}$$

where G is the gravitational constant, c is the speed of light, $B_{lm}(t - \frac{R}{c})$ is a time-dependent amplitude evaluated at the retarded time with dimensions of the second time derivative of the mass quadrupole moment, and T_{ij}^{lm} are transverse–traceless tensor spherical harmonics (Turner 1977a, b). As we have done throughout this work, we restrict ourselves to the $l = 2$ harmonic. For an oscillation mode that generates small perturbations in the mass density, B_{2m} is (Turner 1977b)

$$B_{2m}(t) = \frac{16\pi}{5\sqrt{3}} \frac{{\rm d}^2}{{\rm d}t^2} \int \delta\rho Y_{2m}^* r^2 {\rm d}V, \tag{81}$$

where $\delta\rho$ is the Eulerian perturbation to the mass density. Rearranging equation (12), we obtain an expression for the Eulerian perturbation to the mass density:

$$\delta\rho = -\nabla \cdot (\rho\boldsymbol{\xi}) = -a(t) \times \left(U\frac{{\rm d}\rho}{{\rm d}r} + \rho\left(\frac{{\rm d}U}{{\rm d}r} + \frac{2U}{r} - l(l+1)\frac{V}{r}\right)\right) Y_{lm}. \tag{82}$$

Substituting equation (82) into equation (81) gives

$$B_{2m}(t) = \frac{16\pi}{5\sqrt{3}} \ddot{a}(t) H_n, \tag{83}$$

where we have defined an integral H_n as

$$H_n = -\int \left(U\frac{{\rm d}\rho}{{\rm d}r} + \rho\left(\frac{{\rm d}U}{{\rm d}r} + \frac{2U}{r} - l(l+1)\frac{V}{r}\right)\right) r^4 {\rm d}r, \tag{84}$$

which quantifies an oscillation mode's ability to generate GWs. Note that the only time dependence in equation (83) arises from $\ddot{a}$. We obtain results for the integral H_n for each of our three ocean models. These are displayed in Table 1 in units of g cm^2. Like other integrals computed, H_n is largest in carbon oceans because the carbon ocean is the largest.

We approximate the GW strain $h(t)$ from neutron star ocean tidal waves as

$$h(t) \approx \frac{G}{Rc^4} \frac{16\pi}{5\sqrt{3}} \ddot{a}(t) H_n. \tag{85}$$

We determine at what distance R there would be GW signals with amplitudes $h \sim 10^{-20}$. This is approximately the smallest amplitude detectable with current space-based GW detector technology (LISA Study Team 2000; Robson et al. 2019). We find that GWs from none of the configurations considered will be able to escape the immediate vicinity of the neutron star. The values we report are for the rigid crust models. The configuration that generates the largest GWs is a carbon ocean during a BNS inspiral. The distance from the ocean at which the GWs have an amplitude of $\sim 10^{-20}$ is ∼10 au. In contrast, the smallest GWs are generated in an iron ocean during an NSBH inspiral. In this case, the GW amplitude is $\sim 10^{-20}$ only ∼9 km away. This makes detecting GWs from neutron star ocean tides virtually impossible. While these GWs will serve as a source of extremely weak damping, we find that the damping time-scales are $\gtrsim 10^7$ yr and will not impact neutron star ocean tides on relevant time-scales.

While ocean tidal wave GWs may be undetectable, the orbital motion of these binary systems generates sizable GWs. During the early inspirals of BNSs and NSBHs, GWs will be detectable by *LISA* (LISA Study Team 2000; Robson et al. 2019). GWs from BNS and NSBH mergers are already detected by ground-based GW detectors (LIGO Scientific Collaboration & Virgo Collaboration 2017; LIGO Scientific Collaboration, Virgo Collaboration & KAGRA Collaboration 2021). Consequently, joint detection of GWs with tidally resonant ocean flares remains a possibility for multimessenger astrophysics.

6 CONCLUSION

Neutron star oceans can sustain resonant tides. Though rather small in size, the tidal waves excited in compact binary inspirals and in parabolic encounters possess large amounts of energy, ranging from

Table 3. The estimated distances (in Mpc) out to which flares from neutron star oceans could be detected with *Fermi* or *NuSTAR* assuming isotropic emission. For *Fermi*, X-ray distances are computed assuming $E_\gamma = 8$ keV, while gamma-ray distances are computed assuming $E_\gamma = 40$ MeV. For *NuSTAR*, the lower energy X-ray distances are computed assuming $E_\gamma = 8$ keV, while the higher energy X-ray distances are computed assuming $E_\gamma = 20$ keV. The distances for oceans with elastic crusts are computed by scaling the distances for oceans with rigid crusts by a factor of 0.1.

Ocean	Carbon (rigid)	Oxygen (rigid)	Iron (rigid)	Carbon (elastic)	Oxygen (elastic)	Iron (elastic)
BNS gamma-ray with *Fermi* (Mpc)	3.9	0.82	0.0015	0.39	0.082	0.000 15
BNS X-ray with *Fermi* (Mpc)	280	58	0.11	28	5.8	0.011
BNS higher energy X-ray with *NuSTAR* (Mpc)	520	110	0.20	52	11	0.020
BNS lower energy X-ray with *NuSTAR* (Mpc)	1300	280	0.52	130	28	0.052
NSBH gamma-ray with *Fermi* (Mpc)	2.6	0.55	0.0010	0.26	0.055	0.000 10
NSBH X-ray with *Fermi* (Mpc)	190	39	0.0071	19	3.9	0.000 71
NSBH higher energy X-ray with *NuSTAR* (Mpc)	350	74	0.13	35	7.4	0.013
NSBH lower energy X-ray with *NuSTAR* (Mpc)	900	190	0.34	90	19	0.034

10^{37} to 10^{46} erg, depending on the properties of the neutron star crust. This energy, coupled with the rotational and magnetic energy of a real neutron star, has the potential to break neutron star crusts and fuel electromagnetic flares. Such electromagnetic flares could become early warning signs of merging NSBHs and BNS systems, preceding mergers by $\gtrsim$1 min if neutron star crusts are rigid and $\gtrsim$1 h if the neutron star crusts are elastic. Observations of these flares could shed light on neutron star ocean and crust properties. Their timing relative to compact binary mergers, as well as their duration and oscillation periods may serve as distinct signatures of these flares. Nevertheless, more work is needed to understand the physical mechanisms that can release the energy for flares as well as the effects of rotation and magnetization.

We find that tidally resonant neutron star ocean flares, if in the X-ray band, may be detected at distances of 1−1000 Mpc with *Fermi* and *NuSTAR* in most cases, comparable to the distances of observed BNS and NSBH mergers. We find that X-ray emission could have detection rates as high as $\sim$7 yr^{-1} for BNSs and $\sim$0.6 yr^{-1} for NSBHs. Neutron star ocean tides are consequently a possible source of emission, which can accompany observable GWs. Subsequent work may involve reviewing past *NuSTAR* and *Fermi* data for X-ray bursts in coincident angular locations of observed BNS and NSBH mergers.

Neutron star ocean tides and oscillations may contribute to future multimessenger observations of astrophysical compact binary mergers and neutron stars. Future studies into ocean tidal waves on top of crustal mountains (Gittins & Andersson 2021; Gittins et al. 2021) and resultant neutron star ocean tsunamis may yield interesting results. More exotic systems including collisions between neutron stars and planets may also produce ocean activity that results in multimessenger emission. Multimessenger emission from neutron stars, including emission from ocean tidal waves, will provide new knowledge about the enigmatic but rich physics of neutron stars.

ACKNOWLEDGEMENTS

The authors are grateful to Nils Andersson, Fabian Gittins, Péter Petreczky, Charles Hailey, and Benjamin Owen for very helpful discussions as well as reviewing the manuscript and providing constructive feedback. The authors thank Columbia University in the City of New York and the University of Florida for their generous support. The Columbia Experimental Gravity group is grateful for the generous support of Columbia University. AGS is grateful for the support of the Columbia College Science Research Fellows programme and the Heinrich, CC Summer Research Fellowship. LMBA is grateful for the Columbia Undergraduate Scholars Program Summer Enhancement Fellowship and the Columbia Center for Career Education Summer Funding Program. GOS is grateful for the generous support of the Columbia University Department of Mathematics Research Experience for Undergraduates programme. IPL is grateful for the generous support of the Columbia University Amgen Scholars Program. IB acknowledges the support of the Alfred P. Sloan Foundation and NSF grants PHY-1911796 and PHY-2110060.

DATA AVAILABILITY

The data underlying this article will be shared on reasonable request to the corresponding author.

REFERENCES

Aasi J. et al., 2015, ApJ, 813, 39
Abbott B. P. et al., 2018, Living Rev. Relativ., 21, 3
Abbott B. P. et al., 2019, Phys. Rev. X, 9, 011001
Abbott R. et al., 2022, Phys. Rev. D, 105, 082005
Acernese F. et al., 2015, Class. Quantum Gravity, 32, 024001
Akutsu T. et al., 2019, Class. Quantum Gravity, 36, 165008
Alsing J., Silva H. O., Berti E., 2018, MNRAS, 478, 1377
Amaro-Seoane P. et al., 2017, preprint (arXiv:1702.00786)
Andersson N., 2021, Universe, 7, 97
Andersson N., Kokkotas K. D., 1998, MNRAS, 299, 1059
Andersson N., Pnigouras P., 2020, Phys. Rev. D, 101, 083001
Antoniadis J., Tauris T. M., Ozel F., Barr E., Champion D. J., Freire P. C. C., 2016, preprint (arXiv:1605.01665)
Ascenzi S., Oganesyan G., Branchesi M., Ciolfi R., 2021, J. Plasma Phys., 87, 845870102
Atwood W. B. et al., 2009, ApJ, 697, 1071
Bae Y.-B., Kim C., Lee H. M., 2014, MNRAS, 440, 2714
Baiko D. A., Chugunov A. I., 2018, MNRAS, 480, 5511
Bandari A., 2014, Master's thesis, California State University, Long Beach
Bartos I., Marka S., 2019, Nature, 569, 85
Belczynski K. et al., 2018, A&A, 615, A91
Beloborodov A. M., Li X., 2016, ApJ, 833, 261
Belov K. et al., 2018, Exp. Astron., 46, 241
Bentum M. J. et al., 2020, Adv. Space Res., 65, 856
Bergman J. E. S., Blott R. J., Forbes A. B., Humphreys D. A., Robinson D. W., Stavrinidis C., 2009, preprint (arXiv:0911.0991)
Bildsten L., Cutler C., 1995, ApJ, 449, 800
Bildsten L., Ushomirsky G., Cutler C., 1996, ApJ, 460, 827
Bilous A. V., Watts A. L., 2019, ApJS, 245, 19
Blott R. J. et al., 2013, European Planetary Science Congress, Vol. 8, Space-based Ultra-long Wavelength Radio Observatory (Low Cost) – SURO-LC. European Planetary Science Conference, London, U.K., p. EPSC2013–279

Boonstra A.-J. et al., 2016, IEEE Aerospace Conference, Discovering the Sky at the Longest Wavelengths (DSL), . Institute of Electrical and Electronics Engineers, Piscataway, NJ, p. 1
Brown E. F., Cumming A., 2009, ApJ, 698, 1020
Brown E. F., Bildsten L., Rutledge R. E., 1998, ApJ, 504, L95
Bult P. et al., 2021, ApJ, 907, 79
Cecconi B. et al., 2018, EGU General Assembly Conference Abstracts. EGU General Assembly Conference Abstracts. p. 3648(arXiv:1710.10245)
Chambers F. R. N., Watts A. L., 2020, MNRAS, 491, 6032
Chambers F. R. N., Watts A. L., Cavecchi Y., Garcia F., Keek L., 2018, MNRAS, 477, 4391
Chamel N., Haensel P., 2008, Living Rev. Relativ., 11, 10
Chandrasekhar S., 1957, An Introduction to the Study of Stellar Structure, Vol. 2. Courier Corporation, Chelmsford, MA
Chatziioannou K., 2020, Gen. Relativ. Gravit., 52, 109
Chornock R. et al., 2017, ApJ, 848, L19
Cowling T. G., 1941, MNRAS, 101, 367
Cowperthwaite P. S. et al., 2017, ApJ, 848, L17
De Vittori L., Jetzer P., Klein A., 2012, Phys. Rev. D, 86, 044017
Deibel A., 2016, ApJ, 832, 44
Dommes V. A., Gusakov M. E., 2021, Phys. Rev. D, 104, 123008
Dziembowski W. A., 1971, Acta Astron., 21, 289
Farouki R. T., Hamaguchi S., 1993, Phys. Rev. E, 47, 4330
Ferrari V., 2010, Class. Quantum Gravity, 27, 194006
Ferrari L., Rossi P. C. R., Malheiro M., 2010, Int. J. Mod. Phys. D, 19, 1569
Friedman J. L., Schutz B. F., 1978, ApJ, 221, 937
Fujimoto M. Y., Hanawa T., Iben I. J., Richardson M. B., 1984, ApJ, 278, 813
Galloway D. K., Muno M. P., Hartman J. M., Psaltis D., Chakrabarty D., 2008, ApJS, 179, 360
Geroyannis V. S., Tzelati E. E., Karageorgopoulos V. G., 2017, Int. J. Mod. Phys. C, 28, 1750080
Gittins F., Andersson N., 2021, MNRAS, 507, 116
Gittins F., Andersson N., Pereira J. P., 2020, Phys. Rev. D, 101, 103025
Gittins F., Andersson N., Jones D. I., 2021, MNRAS, 500, 5570
Grimm R. E., 2002, J. Geophys. Res. (Planets), 107, 5006
Grimm R. E., Berdanier B., Warden R., Harrer J., Demara R., Pfeiffer J., Blohm R., 2009, Planet. Space Sci., 57, 1268
Haensel P., Zdunik J. L., 1990, A&A, 227, 431
Haensel P., Zdunik J. L., 2003, A&A, 404, L33
Haensel P., Zdunik J. L., 2008, A&A, 480, 459
Haensel P., Potekhin A. Y., Yakovlev D. G., 2007, in Haensel P., Potekhin A. Y., Yakovlev D. G., eds, Astrophysics and Space Science Library, Vol. 326, Neutron Stars 1 : Equation of State and Structure. Springer, New York, NY
Hansen B. M. S., Lyutikov M., 2001, MNRAS, 322, 695
Hansen C. J., van Horn H. M., 1975, ApJ, 195, 735
Harrison F. A. et al., 2013, ApJ, 770, 103
Haskell B., 2015, Int. J. Mod. Phys. E, 24, 1541007
Heyl J. S., 2004, ApJ, 600, 939
Ho W. C. G., Lai D., 1999, MNRAS, 308, 153
Horowitz C. J., Kadau K., 2009, Phys. Rev. Lett., 102, 191102
Jackson J. D., 1962, Classical Electrodynamics. Wiley, New York
Kaspi V. M., Beloborodov A. M., 2017, ARA&A, 55, 261
Kocsis B., Gáspár M. E., Márka S., 2006, ApJ, 648, 411
Kovacs S. J. J., Thorne K. S., 1978, ApJ, 224, 62
Kozakiewicz J., Kulak A., Kubisz J., Zietara K., 2016, Earth Moon Planets, 118, 103
Kraav K. Y., Gusakov M. E., Kantor E. M., 2021, MNRAS, 506, L74
Krüger C. J., Kokkotas K. D., Manoharan P., Völkel S. H., 2021, Frontiers Astron. Space Sci., 8, 166
Kuan H.-J., Suvorov A. G., Kokkotas K. D., 2021a, MNRAS, 508, 1732
Kuan H.-J., Suvorov A. G., Kokkotas K. D., 2021b, MNRAS, 506, 2985
Lai D., 1994, MNRAS, 270, 611
Lai D., 2012, ApJ, 757, L3
Lander S. K., Andersson N., Antonopoulou D., Watts A. L., 2015, MNRAS, 449, 2047
Lattimer J. M., Prakash M., 2001, ApJ, 550, 426
Lau H. K., Leung P. T., Lin L. M., 2010, ApJ, 714, 1234
Ledoux P., 1974, in Ledoux P., Noels A., Rodgers A. W., eds, Proc. IAU Symp. 59, Stellar Instability and Evolution, International Astronomical Union (IAU), Paris, France, p. 135
Lee U., 2004, ApJ, 600, 914
LIGO Scientific Collaboration, 2015, Class. Quantum Gravity, 32, 074001
LIGO Scientific Collaboration, Virgo Collaboration, 2017, Phys. Rev. Lett., 119, 161101
LIGO Scientific Collaboration, Virgo Collaboration, 2019, Phys. Rev. X, 9, 031040
LIGO Scientific Collaboration, Virgo Collaboration, 2021, preprint (arXiv:2108.01045)
LIGO Scientific Collaboration, Virgo Collaboration, KAGRA Collaboration, 2021, ApJ, 915, L5
LIGO Scientific Collaboration, Virgo Collaboration, KAGRA Collaboration, 2021a, preprint (arXiv:2111.03606)
LIGO Scientific Collaboration, Virgo Collaboration, KAGRA Collaboration, 2021b, preprint (arXiv:2111.03634)
LIGO Scientific Collaboration, Virgo Collaboration, KAGRA Collaboration, 2022a, ApJ, 932, 133
LIGO Scientific Collaboration, Virgo Collaboration, KAGRA Collaboration,, 2022b, Phys. Rev. D, 106, 102008
Lioutas G., Stergioulas N., 2018, Gen. Relativ. Gravit., 50, 12
LISA Study Team, 2000, ESA System and Technology Study Report ESA-SCI, European Space Agency, Paris, France, p. 11
Ma S., Yu H., Chen Y., 2021, Phys. Rev. D, 103, 063020
Mandel I., Broekgaarden F. S., 2022, Living Rev. Relativ., 25, 1
Maraschi L., Cavaliere A., 1977, in Müller E. A., ed., Proc. IAU Symp. 4-1, X-Ray Bursts of Nuclear Origin. Springer, Dordrecht, p. 127
Mathews G. J., Wilson J. R., 1997, ApJ, 482, 929
McDermott P. N., van Horn H. M., Hansen C. J., 1988, ApJ, 325, 725
McWilliams S. T., Levin J., 2011, ApJ, 742, 90
Meisel Z., Deibel A., Keek L., Shternin P., Elfritz J., 2018, J. Phys. G: Nucl. Phys., 45, 093001
Metzger B. D., 2017, Living Rev. Relativ., 20, 3
Metzger B. D., 2019, Living Rev. Relativ., 23, 1
Metzger B. D., Fernández R., 2014, MNRAS, 441, 3444
Metzger B. D. et al., 2010, MNRAS, 406, 2650
Miralda-Escude J., Haensel P., Paczynski B., 1990, ApJ, 362, 572
Mitidis A., 2015, PhD thesis, Univ. Florida
Nicholl M. et al., 2017, ApJ, 848, L18
Osborne E. L., Jones D. I., 2020, MNRAS, 494, 2839
Papa M. A. et al., 2020, ApJ, 897, 22
Passamonti A., Andersson N., 2012, MNRAS, 419, 638
Passamonti A., Bruni M., Gualtieri L., Nagar A., Sopuerta C. F., 2006, Phys. Rev. D, 73, 084010
Passamonti A., Andersson N., Pnigouras P., 2021, MNRAS, 504, 1273
Peters P. C., 1964, Phys. Rev., 136, 1224
Piro A. L., 2012, ApJ, 755, 80
Piro A. L., Bildsten L., 2005a, ApJ, 619, 1054
Piro A. L., Bildsten L., 2005b, ApJ, 629, 438
Press W. H., Teukolsky S. A., 1977, ApJ, 213, 183
Press W. H., Vetterling W. T., Teukolsky S. A., Flannery B. P., 1986, Numerical Recipes, Vol. 818. Cambridge Univ. Press, Cambridge
Prinsloo D. et al., 2018, 12th European Conference on Antennas and Propagation (EuCAP 2018), EMI Modelling of an 80 kHz to 80 MHz Wideband Antenna and Low-noise Amplifier for Radio Astronomy in Space. Institute of Engineering and Technology, London, UK, p. 1
Radice D., Perego A., Hotokezaka K., Fromm S. A., Bernuzzi S., Roberts L. F., 2018, ApJ, 869, 130
Rajan R. T., Boonstra A.-J., Bentum M., Klein-Wolt M., Belien F., Arts M., Saks N., van der Veen A.-J., 2016, Exp. Astron., 41, 271
Randall D. A., 2006, The Nuclear Spectroscopic Telescope Array and the Laser Interferometer Gravitational-Wave Observatory
Reisenegger A., Goldreich P., 1994, ApJ, 426, 688
Robson T., Cornish N. J., Liu C., 2019, Class. Quantum Gravity, 36, 105011
Rosswog S., 2015, Int. J. Mod. Phys. D, 24, 1530012
Roy P., Beri A., Bhattacharyya S., 2021, MNRAS, 508, 2123

Saks N., Boonstra A.-J., Rajan R. T., Bentum M., Beliën F., van't Klooster K., 2010, in The 4S Symposium, Small Satellites Systems and Services, DARIS, a Fleet of Passive Formation Flying Small Satellites for Low Frequency Radio Astronomy. European Space Agency, Madeira Portugal, p. 1
Samuelsson L., Andersson N., Maniopoulou A., 2007, Class. Quantum Gravity, 24, 4147
Soares-Santos M. et al., 2017, ApJ, 848, L16
Spitkovsky A., Levin Y., Ushomirsky G., 2002, ApJ, 566, 1018
Sridhar N., Zrake J., Metzger B. D., Sironi L., Giannios D., 2021, MNRAS, 501, 3184
Strohmayer T., Mahmoodifar S., 2014, ApJ, 793, L38
Suvorov A. G., 2018, MNRAS, 478, 167
Suvorov A. G., Kokkotas K. D., 2020, Phys. Rev. D, 101, 083002
Taylor G. I., 1936, Proc. R. Soc. A, 156, 318
Tsang D., 2013, ApJ, 777, 103
Tsang D., Read J. S., Hinderer T., Piro A. L., Bondarescu R., 2012, Phys. Rev. Lett., 108, 011102
Turner M., 1977a, ApJ, 216, 610
Turner M., 1977b, ApJ, 216, 914
Urpin V., 2004, A&A, 421, L5
Ushomirsky G., Cutler C., Bildsten L., 2000, MNRAS, 319, 902
van Baal B. F. A., Chambers F. R. N., Watts A. L., 2020, MNRAS, 496, 2098
Vietri M., 1996, ApJ, 471, L95
Wang L.-J., Tan L., Li Z., Misch G. W., Sun Y., 2021, Phys. Rev. Lett., 127, 172702
Wen D.-H., Li B.-A., Chen H.-Y., Zhang N.-B., 2019, Phys. Rev. C, 99, 045806
Woosley S. E., Taam R. E., 1976, Nature, 263, 101
Yakovlev D. G., Pethick C. J., 2004, ARA&A, 42, 169
Yang H., East W. E., Paschalidis V., Pretorius F., Mendes R. F. P., 2018, Phys. Rev. D, 98, 044007
Ye C. S., Fong W.-f., Kremer K., Rodriguez C. L., Chatterjee S., Fragione G., Rasio F. A., 2020, ApJ, 888, L10

This paper has been typeset from a TEX/LATEX file prepared by the author.